Applied Surface Science Advances 30 (2025) 100906

Contents lists available at ScienceDirect

Applied Surface Science Advances

journal homepage: www.sciencedirect.com/journal/applied-surface-science-advances

Full Length Article

Enhancing hydrophilic properties of spherical C(sp^2)-hybridized carbon nanostructures through the targeted oxidation of their outer layer

Marta E. Plonska-Brzezinska [a,*], Joanna Breczko [b], Damian Pawelski [a], Julio César Zuaznabar Gardona [c], Alex Fragoso [c], Krzysztof Brzezinski [d], Artur P. Terzyk [e]

[a] Department of Organic Chemistry, Faculty of Medicine with the Division of Dentistry and Division of Medical Education in English, Medical University of Bialystok, Mickiewicza 2A, 15-222 Bialystok, Poland
[b] Faculty of Chemistry, University of Bialystok, Ciolkowskiego 1K, 15-245 Bialystok, Poland
[c] Departament d'Enginyeria Química, Universitat Rovira i Virgili, Avda. Països Catalans, 26, 43007 Tarragona, Spain
[d] Department of Structural Biology of Prokaryotic Organisms, Institute of Bioorganic Chemistry, Polish Academy of Sciences, Noskowskiego 12/14, 61-074 Poznan, Poland
[e] Faculty of Chemistry, Nicolaus Copernicus University in Torun, Gagarin Street 7, 87-100 Torun, Poland

ARTICLE INFO

Keywords:
Carbon nanostructure
Carbon nano-onion
sp^2-hybridized carbon
Oxidation
Functionalization
Dispersion
Polar solvent

ABSTRACT

Oxidation processes affect the structural integrity of carbon nanostructure (CN), leading to changes its physicochemical properties, as a result of oxidation of sp^2-hybridized carbon atoms, and formation of appropriate functional groups, further determining the surface properties of CNs. This work used several oxidation methods to develop effective procedures for the selective modification of the carbon nano-onion (CNO). Hydrogen peroxide, urea hydrogen peroxide complex, acetic chloride or anhydride, and trifluoroacetic acid were used as the primary reagents in various configurations for the functionalization of CNOs, which resulted in the formation of oxygen-containing groups, mainly carbonyls, phenolic, carboxyl, ethers, and esters. The dispersion of functionalized CNOs was tested in a series of protic, aprotic polar, and nonpolar solvents that were used to determine the Hansen Solubility Parameters. The dispersion of oxidized CNOs was determined experimentally in water, by designating the zeta potential of dispersed CNOs and their diameters using dynamic light scattering. The formation of oxygen-containing groups ensures high dispersion of CNs in polar solvents and provides high stability in water for more than two months. It is the first work describing such effective methods of functionalizing spherical nanostructures containing C(sp^2)-hybridized carbon atoms, where the dispersion stability in water is so significant.

1. Introduction

Selective oxidation is a key route to tailor the physicochemical properties of carbon nanostructures (CNs). By converting selected sp^2-hybridized carbons into oxygen-containing moieties, oxidation governs surface energy, solvent interactions, and ultimately dispersibility, properties central to applications in catalysis and energy storage. Because these surface groups also arise alongside lattice oxidation, understanding how specific oxidation chemistries sculpt CN structure and interfacial behaviour is essential for rational design.

Using CNs in many areas requires their high dispersibility in polar solvents. Due to van der Waals and π-π stacking interactions and an amorphous carbon on their surface, CNs tend to form large aggregates that hinder their separation and usage [1]. Modifying their surface is one of the most straightforward approaches to decreasing their aggregation and increasing their dispersibility. The most frequent method is based on the chemical oxidation of CNs using concentrated inorganic acids, such as nitric acid or a mixture of nitric and sulphuric acids [2–6]. The oxidative treatment completely removes amorphous carbon from the CN surface, leading to some structural degradations of the nanostructure. It simultaneously introduces oxygen-containing functionalities, enhancing CNs dispersibility in polar solvents. Although this simple modification effectively increases dispersibility, it has some crucial limitations. This uncontrolled functionalization causes damage and structural changes to the integrity of the CN surface, which in turn has a destructive effect on its physical and chemical properties. Additionally, the process leads to

* Corresponding author.
E-mail address: marta.plonska-brzezinska@umb.edu.pl (M.E. Plonska-Brzezinska).

https://doi.org/10.1016/j.apsadv.2025.100906

Available online 27 November 2025

the adsorption of inorganic ions, which are challenging to desorb [7,8].

The modification of the CN surface mainly concerns wet chemical oxidation [9,10]. The method uses, apart from the acids mentioned above, other reagents with oxidizing properties, such as $KMnO_4$ [6], H_2O_2 [11,12], ozone [9,13,14], or $(NH_4)_2S_2O_8$ [15]. In addition to the classic oxidation method, it is also used in constant-potential electrolysis [16], sonochemical treatment [17] or plasma treatment [18,19], etc. In effect, these oxidative processes can generate various oxygenated functional groups on the CN surface, such as aldehydes, ketones, epoxides, esters, alcohols, and carboxylic acid moieties (the last two mentioned are the most common) [10,9,13,20]. Still, the nature of these groups is somewhat random, and uncontrollable. It has also been noted that in many cases, oxidative treatment is the first step in further modification with other chemical moieties. The nature of the functional groups containing oxygen is essential because it determines the following stages of possible reactions and further functionalization. The product's chemical purity after oxidative modifications is also critical. Considering all the above-mentioned factors, the functionalization process of CNs aimed at increasing dispersity by creating oxygen-containing groups on the nanostructure's surface should be designed in detail.

A persistent gap in the literature is the lack of head-to-head comparisons: many studies introduce new oxidation methods sequentially, without rigorous cross-evaluation of products under unified conditions. Here, in addition to established protocols, we introduce several new surface-functionalization routes that target specific oxygen functionalities on CNs, enabling selective oxidation with improved control over product composition.

It should be emphasized that multi-layered fullerenes have a chemical composition similar to carbon nanotubes, graphite, or graphene due to the excessive presence of sp^2-hybridized carbon atoms and defects in the structure, which are active sites of chemical reactions. Since multi-layered fullerenes have many features similar to other CNs, we carried out the oxidation reactions on the spherical structure of multi-layered fullerenes (carbon nano-onions, CNOs) [21–23], which serve CNOs as an appropriate model system. Herein, we used CNOs with a diameter of approximately 5–9 nm that were formed by the thermal annealing of nanodiamond (ND) particles [24–27]. CNOs were selected as the sp^2-carbon model because they combine high electrical conductivity, a fully accessible external surface, nanometer dimensions, and scalable synthesis from NDs, enabling precise control of defect density and surface chemistry. Their spherical, multi-layered graphitic architecture reduces bundling compared with nanotubes, simplifies dispersion analysis, and provides a uniform platform for comparing oxidation routes targeted to specific oxygen functionalities. CNOs also present constraints. Curvature-induced strain can shift oxidation pathways relative to planar graphene; concentric shells limit access to inner layers; and as-prepared materials may be polydisperse with low intrinsic porosity. We address these factors by focusing on outer-shell functionalization, reporting size distributions and defect metrics, and benchmarking dispersibility under matched conditions. CNOs offer a practical and representative nanostructure within these boundaries for selective oxidation. Finally, the availability of large-scale synthesis and robust post-synthetic modification further supports their selection, with demonstrated relevance across electrochemical energy storage [28–31], catalysis [32–34], electrocatalysis [35–37], and biomedicine [38–40].

Oxidation outcomes depend sensitively on multiple parameters, including pre-existing heteroatoms or adsorbates, purity and porosity, graphitic character, defect density, and surface chemical state [41]. We therefore implement a set of CNO oxidation protocols in which the oxidant, reaction environment, and exposure are tightly controlled to yield oxidized CNOs (ox-CNOs) with predefined surface functionalities. Systematic structure–property analysis links each method to the resulting defect landscape, functional-group distribution, and dispersion behaviour in polar solvents. This framework identifies efficient, reproducible routes to ox-CNOs that maximize dispersibility while preserving structural integrity and minimizing inorganic contamination.

This work introduces selective oxidation strategies that steer CNO surfaces toward predetermined oxygen functionalities, overcoming the random, damage-prone outcomes of conventional methods; it offers the first unified, side-by-side comparison of multiple oxidation routes under matched conditions, directly linking reaction chemistry to defect formation and dispersibility; and it minimally damaged ox-CNOs with tunable surface groups, enabling reliable downstream functionalization and improved processing for catalysis and energy-related applications. Collectively, these advances establish controllable, scalable pathways to application-ready functionalization of sp^2-hybridized CNs.

2. Experimental section

2.1. Materials and chemicals

Nanodiamond powder (ND) with crystal sizes between 4–6 nm and content greater than 97 wt.% (μDiamond®Molto, Carbodeon) was used for the preparation of CNOs. Molecular sieves (4 Å MS; POCH Poland) were dried by annealing with an open flame before use. Triethylamine (TEA, >99 %; POCH Poland) was purified by distillation under Ar over KOH flakes. The distillate was poured into a dark glass bottle with the addition of freshly roasted 4 Å MS (10 % by w/w). Fullerene C_{60} (98 %, Merck, Germany), 1,8-diazabicyclo[5.4.0]undec-7-ene (DBU, ≥98 %, Merck, Germany), trimethylamine hydrochloride (Me_3N, 98 %, Merck, Germany), tripropylamine (iPr_3N, ≥99 %, Merck, Germany), tributylamine (n-Bu_3N, ≥98 %, Merck, Germany), triethylamine (Et_3N, ≥98 %, Merck, Germany) *N,N*-diisopropylethylamine (DIPEA, 99.5 %, Merck, Germany), *N,N,N′,N′*-tetramethylethylenediamine (TMEDA, ≥99 %, Merck, Germany), *N*-methylmorpholine (NMM, ≥98 %, Merck, Germany), 2,2,6,6-tetramethylpiperidine (TMP, ≥97 %, Merck, Germany), *N,N*-dimethylpyridin-4-amine (DMAP, ≥99 %, Merck, Germany), *N,N*-dimethylaniline (≥99 %, Merck, Germany), *N,N*-diethylaniline (≥99 %, Merck, Germany), pyridine (99.8 %, Merck, Germany), urea (≥99.5 %, Merck, Germany), tetrabutylammonium bromide (Bu_4NBr, ≥98 %, Merck, Germany), tetrabutylammonium hydroxide (Bu_4NOH, ≥98 %, Merck, Germany), tetrabutylammonium hydrogen sulphate (Bu_4NHSO_4, ≥98 %, Merck, Germany), urea hydrogen peroxide complex (UHP, 97 %, Merck, Germany), 3-chloroperbenzoic acid (mCBPA, <77 %, Merck, Germany), acetic chloride (AcCl, 98 %, Merck, Germany), acetic anhydride (Ac_2O, ≥98 %, Merck, Germany), acetic hydroxide (AcOH, ≥98 %, Merck, Germany), acetic chloride (AcCl, ≥98 %, Merck, Germany), trifluoroacetic acid (TFA, ≥99 %, Merck, Germany), trifluoroacetic anhydride (TFAA, ≥9 %, Merck, Germany), anhydrous aluminium chloride ($AlCl_3$, 98 %, Merck, Germany), hydrogen peroxide (60 % H_2O, Aneva, Poland), sodium hypochlorite (15 % H_2O, Warchem, Poland), acetic acid (>99 %, POCH, Poland), potassium carbonate (>98 %, POCH, Poland), sodium hydroxide (>98 %, POCH, Poland), magnesium sulfate (>98 %, POCH, Poland), sodium thiosulfate (98 %, POCH, Poland), molecular iodine (>99 %, POCH, Poland), sulfuric acid (>98 %, POCH, Poland). 2-Propanol (IPA), acetone, hexane, toluene, *tert*-buthanol, ethanol (EtOH, 96 %), acetonitrile (MeCN) were purchased from POCH (Poland) and then purified by fractional distillation before use. Tetrahydrofuran (THF) and 1,2-dichloroethan (DCE) were purchased from POCH (Poland) and then purified by fractional distillation over phosphorous pentoxide. Anhydrous THF was obtained after additional simple distillation over the ketyl radical (sodium/benzophenone).

2.2. Synthetic procedures

2.2.1. Preparation of pristine-CNOs from NDs using thermal annealing

Commercially available, nanodiamond powder (ND) with crystal sizes between 4–6 nm and content greater than 97 wt.% (μDiamond®Molto, Carbodeon) was used for the preparation of pristine CNOs (p-CNOs). Annealing of NDs was performed at 1650 °C under a 1.1 MPa He atmosphere (20 °C min^{-1}) using carbonization furnace. The final

temperature was maintained for one hour, and then the material was annealed in air at 400 °C to remove amorphous carbon from the obtained material.

2.2.2. Procedure of the functionalization of p-CNOs

p-CNOs were functionalized with P1-P11 procedures (please see SI for a detailed description of the procedures). P7 and P11 were made under the same experimental conditions, with the difference that the substrate was a different starting material; therefore, sequential numbering was introduced to distinguish the reaction products. Table 1 summarizes p-CNO functionalization, with the leading reagent indicated in a chemical reaction and the abbreviations that will be used for the products of individual chemical reactions. In brief, the dominant functional groups identified based on X-ray photoelectron spectroscopy (XPS) are included. To facilitate further identification of individual ox-CNOs, in the further discussion, we use designations indicating the number of dominant functional groups in the material and, in brackets, the number of functionalization procedures summarized in Table 1 and described below.

Procedure 1. (P1): To a 30 mL glass microwave (MW) tube, 30 mg of CNO, 1.0 g UHP, 0.5 mL Et_3N, and 10 mL of the IPA/H_2O mixture (8:2, v/v) were added [42,43]. The tube was capped and sonicated at room temperature (RT) for 10 min, then heated under MW at 60 °C for 8 h. Then, distilled water was added to the reaction mixture, the suspension was centrifuged, and the supernatant was decanted. The solid residue was then washed with several solvents, and the resulting precipitate was dried under vacuum to give 29 mg of a black solid.

Procedure 2. (P2): To a 30 mL glass tube, 30 mg of CNO, 200 mg of mCPBA, and 20 mL of anhydrous DCE were added [44]. The tube was purged with Ar, sealed, sonicated for 1 h at 60 °C, and then magnetically stirred for 12 h. Next, to the reaction mixture, hexane was added, the suspension was centrifuged, the supernatant decanted, and the solid was washed with several solvents. The obtained product was dried under vacuum to give 30 mg of a black solid.

Procedure 3. (P3): To a 50 mL round-bottom flask, 30 mg of CNO was added, 10 mL of AcOH, 20 mg of molecular iodine, and then 0.20 mL of concentrated H_2SO_4. The flask was cooled in an ice bath to 0 °C, and then, 10 mL of 30 % H_2O_2 solution was added dropwise. The suspension was sonicated at RT for 1 h, and then heated at 60 °C overnight. To the reaction mixture, 5 % Na_2SO_3 solution was added, sonicated for 5 min at RT, and then centrifuged on a rotary centrifuge. The liquid was decanted from the precipitate and was washed with distilled water and acetone to give 29 mg of a black solid.

Procedure 4. (P4): To a 50 mL PP tube, 30 mg of CNO, 2 mL of 60 % water solution of H_2O_2, 1 mL of 1 M NaOH, 100 mg of *n*-Bu_4NBr, and 0.50 mL of DBU were added. The suspension was sonicated at RT for 1 h, then stirred magnetically for 24 h. Next, acetone was added, and the carbon material was centrifuged. A liquid was decanted from the precipitate, and the solid residue was washed with 5 % AcOH, distilled water, and acetone. Finally, the product was dried under a vacuum to produce 30 mg of a black solid.

Procedure 5. (P5): To an intensively stirred 70 % solution of H_2SO_4 (8.75 mL) at 0 °C, *tert*-BuOH (12 mL) was added dropwise, and then a 30 % solution of H_2O_2 (20 mL) was added dropwise during 1 h. The mixture was stirred at RT for 12 h. Next, the aqueous layer was discarded, the organic layer was washed with a saturated NaCl solution, and the extract was dried with anhydrous $MgSO_4$. Next, 30 mg of CNO, 20 mL of DCM, and 2.0 mL of DBU were added to the filtrate. The reaction mixture was sonicated at RT (1 h) and heated at 60 °C overnight. The suspension in hexane was centrifuged, and the residue was then washed with hexane and methanol to give 26 mg of a black solid.

Procedure 6. (P6): The reaction was performed under anhydrous conditions under an Ar atmosphere. The 50 mg of CNO, freshly powdered $AlCl_3$ (1.56 g, 11.8 mmol), and 50 mL of anhydrous DCM were added to a 100 mL round-bottom flask. The resulting suspension was sonicated for 10 min at RT, and after cooling in an ice bath to 0 °C, AcCl (0.70 mL, 9.8 mmol) was added dropwise. The reaction mixture was sonicated at the set temperature for 2 h, and then stirred at RT (12 h). Next, the dry content was transferred with 10 % AcOH solution, and the product was centrifuged. The supernatant was decanted from the precipitate, which was then washed with several solvents to give 54 mg of a black solid.

Procedure 7. (P7): The product from modification (**6**) (20 mg) was oxidized by 15 % NaClO solution (15 mL) at RT. The resulting suspension was sonicated for 2 h at 0 °C. Then, 10 % $Na_2S_2O_3$ solution (20 mL) was added and acidified with 1 M HCl to pH 4–5. The carbon material was centrifuged, the liquid was decanted from the precipitate, and the solid residue was washed with distilled water and acetone to give 18 mg of black solid.

Procedure 8. (P8): [HTEA]CF_3CO_2 (0.5 g) [45], UHP (2.0 g), 30 mg CNO, 50 mL THF were added to a 100 mL round-bottom flask, equipped with a 0 °C sonication bath, followed by drops of TFAA (1.51 g, 1.0 mL) [43]. The mixture was sonicated at the set temperature for 2 h and then at RT for 1 h. Then, the distilled water (20 mL) was added, the suspension was centrifuged, the liquid was decanted from the precipitate, and the solid residue was washed with a mixture of H_2O/acetone. Finally, the resulting carbon material was dried under vacuum to give 30 mg of black solid.

Procedure 9. (P9): Na_2CO_3•1.5 H_2O_2 (1.0 g), 30 mg CNO, 50 mL of THF/DCM (1:1, v/v) mixture was sonicated at 0 °C (1 h), followed by drops of TFAA (1.51 g, 1.0 mL). Next, the mixture was stirred at RT for 12 h. Then the reaction mixture was centrifuged on a rotary centrifuge. The liquid was decanted from the precipitate, and the solid residue was then washed with several solvents to give 29 mg of a black solid.

Procedure 10. (P10): The reaction was carried out under anhydrous conditions and an Ar atmosphere. 50 mg of CNO and 15 mL of Ac_2O were added to a 30 mL round-bottom flask. The suspension was cooled in an ice bath to 0 °C, and 1.5 g of powder anhydrous $AlCl_3$ was added in

Table 1
Summary of the type of the modifications of CNOs based on XPS studies.

Substrate	Procedure	Main reagents	Product/ Abbreviation
ND Molto	Thermal treatment		p-CNO
p-CNO	P1	UHP, Et_3N, IPA/H_2O	CNO>O/OH(**P1**)
	P2	mCPBA, DCE	CNO>O(**P2**)
	P3	AcOH, I, H_2SO_4, 30 % H_2O_2	CNO>O/OH(**P3**)
	P4	60 % H_2O_2, *n*-Bu_4NBr, DBU	CNO>O/OH(**P4**)
	P5	30 % H_2O_2, *tert*-BuOH, 70 % H_2SO_4	CNO>O(**P5**)
	P6	AcCl, DCM	CNO>O/COOR (**P6**)
CNO>O/COOR (**P6**)	P7	15 % NaClO	CNO>O/COOH (**P7**)
p-CNO	P8	[HTEA]CF_3CO_2, UHP, TFAA	CNO>O/COOH (**P8**)
	P9	Na_2CO_3· H_2O_2, TFAA, THF/DCM	CNO>O/OH(**P9**)
	P10	Ac_2O	CNO>O/COOR (**P10**)
CNO>O/COOR (**P10**)	P11	15 % NaClO	CNO—COOH (**P11**)

portions. The suspension was sonicated at RT for 1 h and refluxed for 12 h. Then, 50 g of crushed ice was added, and the carbon material was centrifuged. Finally, the resulting carbon material was dried under vacuum to give 51 mg of a black solid.

Procedure 11. (analogous to P7): 20 mg of the product (**10**) and 15 % NaClO solution (10 mL) (cooled to 0 °C), and the resulting suspension was sonicated for 2 h at 0 °C. Then, 10 % $Na_2S_2O_3$ solution (20 mL) was added and acidified with 1 M HCl to pH 4–5. The carbon material was centrifuged, and the solid residue was washed with distilled water and acetone. The carbon material was dried at RT under reduced pressure to give 19 mg of a black solid.

2.3. Determination of Hansen solubility parameters for ox-CNOs

To assess the dispersion behaviour of ox-CNO, their HSPs (δ_D, δ_P and δ_H) were determined as previously described for p-CNOs [46]. Briefly, 3 mg of each CNO sample was mixed with 3 mL of a selected solvent (see Table S5 for the complete solvent list) in a glass vial. The mixture was then sonicated in an ultrasonic bath (40 kHz, 110 W) for one hour. After sonication, the dispersibility of ox-CNOs in each solvent was assessed qualitatively. A score of 1 was assigned for good dispersions and 0 for poor dispersions. The resulting dispersibility data were then fitted using the algorithm developed by Gharagheizi to estimate the corresponding Hansen Solubility Parameter (HSP) values [47]. The interactions between ox-CNOs and the tested solvents were further quantified using the solubility parameter distance (R_a) and the Relative Energy Difference (RED) according to Eqs. (1) and 2, respectively [48].

$$R_a = \sqrt{4\left(\delta_{D_{CNO}} - \delta_{D_{SOLVENT}}\right)^2 + \left(\delta_{P_{CNO}} - \delta_{P_{SOLVENT}}\right)^2 + \left(\delta_{H_{CNO}} - \delta_{H_{SOLVENT}}\right)^2} \quad (1)$$

$$RED = \frac{R_a}{R_0} \quad (2)$$

where δ_D, δ_P and δ_H represent the HSPs for the CNOs and the solvent, and R_0 is the interaction radius, defining the maximum interaction difference between the solute and solvent. A RED value <1 ($R_a < R_0$) indicates a relatively strong interaction between the CNOs and the solvent, whereas a *RED* value greater than 1 suggests a weak interaction.

3. Results and discussion

3.1. Determining the conditions for CNOs functionalization based on the reaction with fullerene C_{60}

Some of the procedures developed in this study were adapted from literature reports on analogous oxidation reactions of fullerene C_{60}. Reaction conditions were subsequently modified to suit CNOs, considering their larger surface area and lower curvature compared to C_{60}. As highlighted by Hirsch [49], the efficiency of CNs functionalization depends not only on the hybridization state of surface carbon atoms but also on their curvature. Because CNOs possess a significantly lower curvature than C_{60}, higher concentrations of oxidants and surface-modifying reagents are necessary to achieve comparable functionalization degrees. The detailed synthetic procedures are provided in the Supporting Information and summarized in Tables S1 and S2, while the main findings are discussed below.

Fullerene C_{60} was first used as a model system to identify efficient oxidative functionalization routes. In addition to conventional oxidants reported for CN oxidation [50–55], our approach employed aqueous H_2O_2 as the primary oxidant (Table S1). Previous studies demonstrated that heating C_{60} in 30 % H_2O_2 at 60 °C for 2–12 days, in the presence of an interfacial transfer catalyst such as Bu_4NOH and Et_3N in a biphasic water/toluene system, yields highly oxidized products [51]. Under optimized conditions, this process can be shortened to 30 min. In the present work, we achieved a remarkable acceleration by increasing the H_2O_2 concentration, introducing catalytic amounts of MeCN, and replacing Et_3N with Bu_4NHSO_4 as the phase-transfer catalyst (Table S2). These modifications reduced the reaction time from 30 min to only 20 s, marking a significant advance in the oxidative functionalization of both C_{60} and CNOs.

Mechanistically, tertiary amines were found to play a critical role (Table S2). They react with H_2O_2 to form *N*-oxides that coordinate with H_2O_2, promoting the formation of epoxides on the carbon surface. Comparative experiments indicated that amine basicity is the key parameter controlling catalytic performance, with DBU showing the highest activity. In contrast, sterically hindered amines such as DIPEA and TMEDA exhibited lower efficiency, likely due to the restricted formation or stabilization of *N*-oxides. The presence of MeCN further enhanced oxidation through the formation of reactive peroxycarboximidic intermediates [56,57]. Together, MeCN and strongly basic tertiary amines significantly increased oxidation rates compared to NaOH or conventional quaternary ammonium salts, confirming that phase-transfer catalysis via amine *N*-oxides is more effective than classical quaternary systems. Moreover, n-Bu_4NBr was observed to further accelerate oxidation by improving HO_2^- transfer between phases [58], though limited CNO dispersibility in nonpolar solvents remains a challenge. NaOH also facilitated epoxide ring-opening to diols, in agreement with prior reports for polymers and simple epoxides [59,60].

From a broader chemical perspective, the oxidative systems employed here draw on concepts of metal-free oxidation known from organic synthesis, which have been adapted for fullerene chemistry. Reagents such as TFAA and UHP have been shown to function as mild oxidants under green conditions, offering sustainable alternatives to metal-based systems. TFAA, typically an acylating reagent, can also induce oxidation of tertiary amines to *N*-oxides via hydrogen transfer [61,62], and, when combined with DMSO, facilitates the oxidation of alcohols to β-diketones [63]. Similarly, UHP in the presence of tertiary amines efficiently converts benzylic alcohols to carboxylic acids under solvent-free, MW-assisted conditions, exemplifying atom-efficient and environmentally benign oxidation. Acetyl derivatives, including acetic anhydride, hydroxide, and chloride, have also been employed as auxiliary oxidants in analogous systems [64,65].

Overall, this study presents a novel, ultrafast, and metal-free oxidation protocol for the functionalization of C_{60} and CNOs, utilizing a synergistic combination of H_2O_2, MeCN, and Bu_4NHSO_4 under mild conditions. The novelty lies in coupling tertiary amine catalysis, interfacial transfer, and nitrile activation, enabling near-instantaneous oxidation while adhering to the principles of green chemistry. This method offers a novel, sustainable, and highly efficient route for the surface oxidation of CNs, thereby expanding the scope of environmentally friendly oxidation strategies to nanostructured carbon.

3.2. Structural properties of functionalized CNOs using HRTEM and XRD studies

The CNO nanostructures were prepared from ND particles using thermal treatment under reduced pressure and an inert atmosphere using the modified Kuznetsov method [24]. Under these experimental conditions, the ND structures with neighboring layers with a distance of about 0.22 nm transform into spherical concentric graphitic shells of p-CNO [66]. High-resolution transmission electron microscopy (HRTEM) enables detailed imaging of CNs and the evolution of their curved graphitic layers as a function of CNOs chemical treatment (Figs. 1 and S5). HRTEM observations of p-CNOs showed spherical carbon structures formed aggregates ranging between 3 and 40 nm diameters with a significant predominance of spherical 'small' systems with a diameter of approximately 5–9 nm (Fig. 1a). Graphitic shells surround the central fullerene at the CNO core with an intershell spacing around 0.34 nm [67,68], similar to highly ordered pyrolytic graphite (HOPG) [69].

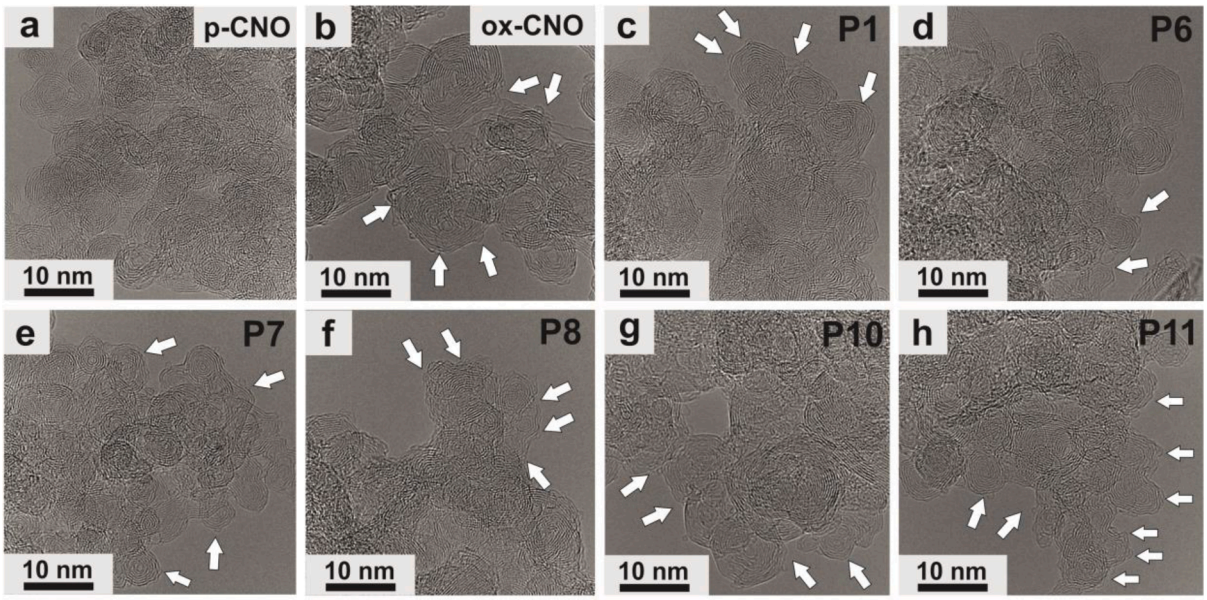

Fig. 1. Representative HRTEM images of (a) p-CNOs functionalized using (b) 3 M HNO_3 (ox-CNOs), procedures (c) P1, (d) P6, (e) P7, (f) P8, (g) P10 and (h) P11.

Chemical treatment with the oxidizing agents appears to lead to CNO's functionalization with varying effectiveness. HRTEM imaging shows an interruption of the CNO layers, graphitization or even the appearance of graphitic nanoribbons. The amount and type of structural defects formed depend on the oxidizing agent used and the conditions for carrying out this process, which are briefly summarized below. Oxidation with concentrated HNO_3 most commonly yields heavily defected CNOs spanning a range of diameters (Fig. 1b). In HRTEM images (white arrows), outer graphene shells are torn, producing shell discontinuities and distortions that disrupt the spherical morphology. The resulting nanoparticles are polydisperse in size and shape. While this treatment affords materials that disperse readily in polar solvents, it is poorly suited for studies requiring strict control over particle size or preservation of the outermost graphene layer. Oxidation perturbs the integrity of graphitic shells in CNOs, with the extent of damage governed by the oxidation protocol and oxidant strength (Table 1). To rationally design hydroxylation strategies for multi-layered fullerenes, we first used C_{60} (single-layer fullerene) as a model, given its curvature-driven reactivity closely resembling that of CNOs [70]. Curvature generally enhances the chemical reactivity of CNs [71]. In fullerenes, atoms adjacent to pentagons exhibit increased pyramidalization and strain, which modify local electron density and facilitate nucleophilic attack and related reactions compared with planar graphitic lattices [71,72]. As curvature increases, reactivity rises accordingly, promoting transformations such as oxidation and cycloaddition [72]. A detailed description of the C_{60}-based oxidation protocols and their subsequent translation to CNOs is provided in the Supporting Information.

HRTEM studies show that only in the case of modification using P3 (product CNO>O/OH(3)) is a non-homogeneous material formed, in which CNO particles and graphitic nanoribbons coexist (Fig. S5b). The experimental conditions led to the destruction of some CNO's spherical structures, and the formation of graphitic nanoribbons was observed, which other authors also noticed, where the oxidized CNs can serve as precursors for synthesizing ribbon-like geometries [73,74]. For instance, the edges of oxidized CNs possess functionalities that promote further polymerization or cross-linking, which is essential for ribbon formation. Additionally, oxidation processes can modify the electronic properties of CNs, allowing for the selective activation of edges and defect sites, which is crucial for the subsequent rearrangement of carbon atoms into nanoribbons. Curved soot particles are oxidized more easily than planar ones, and the oxidation rate depends significantly on the curvature and structural modifications induced by the oxidative environment [72,75]. It should also be emphasized that in the case of P3, a unique reaction environment was created to form pyrene-like radicals of CNs using simultaneously iodine, concentrated H_2SO_4, and H_2O_2. Iodine has been known to act as a Lewis acid in some chemical contexts, facilitating the activation of monomers for polymerization reactions. Additionally, iodine enhances the electron-withdrawing ability of carbonyl groups in carbon compounds, facilitating reactions such as the Diels–Alder reaction, which can be relevant in polymerization mechanisms involving conjugated systems [76]. In concentrated acidic environments, molecular iodine can catalyze reactions by generating reactive iodine species, potentially leading to radical formation. Research indicates that when combined with H_2O_2, radicals can be generated - hydroxyl radicals and iodine radicals [77]. These radicals are critical initiators in radical polymerization mechanisms, setting the stage for transforming small molecular precursors or functionalized carbon substrates into larger polymeric structures. All these factors resulted in the competitive formation of ribbon-like structures during the oxidation reaction of CNOs. This method also seems less valuable due to the need for more control over the resulting material in correlation to its structure and homogeneity.

Two successive outer layers in ox-CNOs, presented in Fig. 1, show the breaking of the continuity of graphitic layers. Most of these nanostructures retained their spherical shape. However, some have a deformed spherical shape, which manifests in specific distortions. It is most visible in HRTEM images of nanostructures oxidized using the P8 (Fig. 1f) and P10 (Fig. 1g) methodologies. Additionally, spherical nanostructures with smaller diameters are obtained using P7 (Fig. 1e) and P11 (Fig. 1h). Two subsequent modification reactions led to the formation of the product as a result of P7 (substrate - CNOs oxidized as a result of P6) and P11 (substrate - CNOs oxidized as a result of P10). Decreasing the diameter of CNOs oxidized indicates that multiple processes lead to some "chemical peeling" of multi-layered fullerenes, forming CNs with a smaller diameter.

X-ray diffraction (XRD) is the standard method for crystal structure analysis. The diffraction patterns for selected CNs are presented in Fig. 2. The diffraction patterns of NDs, p-CNOs, and ox-CNOs (3 M HNO_3) are presented as reference materials (Fig. 2a). The three phases of CNs are visible during X-ray diffraction with different intensities, which enables their structural analysis. For NDs, three primary reflexes are observed at 2θ equal to 43.5° (111), 75.8° (220), and 92.0° (311), which correspond

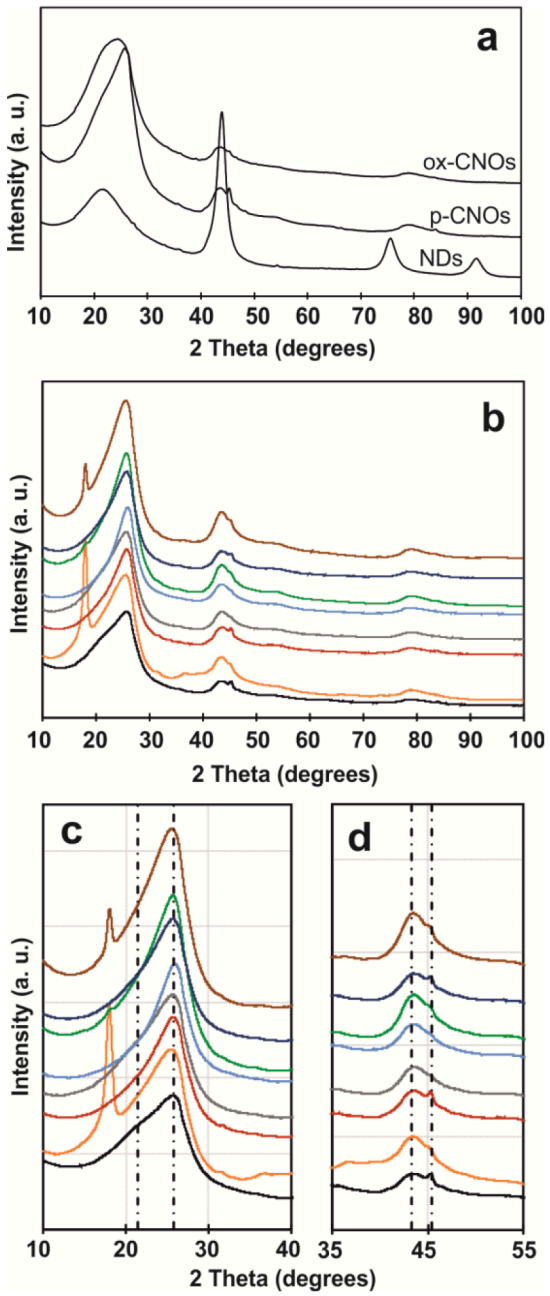

Fig. 2. XRD patterns of (a) NDs, p-CNOs and ox-CNOs (3 M HNO_3), (b-d) p-CNOs and these functionalized using procedure P1 (orange), P2 (red), P6 (gray), P7 (blue), P8 (green), P10 (dark blue) and P11 (brown).

to diamond-like phases (Fig. 2a), the first of which is characterized by the greatest intensity [67]. The reflex at 2θ equal to 22° corresponds to the (002) peak of graphite and, therefore, suggests that there may be some contribution from small quantities of sp^2-bonded carbon atoms. The surface of the NDs is considered to be terminated by sp^2-like bonding [67,78]. This peak at 2θ equals 25.3° (002), and the second at 2θ equals 43.4° (100) are characteristics for p-CNOs (Fig. 2a) that are characteristic of hexagonal graphite. The most apparent change in the pattern is the growth of a broad graphite peak (002). The NDs have been converted from a sp^3-bonded structure to one containing many sp^2-bonded carbon atoms. The broadening of this peak indicates the presence of sp^2-hybridized carbon atoms and those atoms with sp^3/sp^2 hybridization. This broadening is also related to the size of the crystallites, and to the presence of strains and defects [78].

Although the diffraction patterns for ox-CNOs did not show significant differences, the profiles indicate the presence of a mixture of the different phases containing diamond- and graphitic-like domains. For all carbon materials, the most substantial asymmetric broad reflection was observed at $2\theta = 25.3°$, with an asymmetric broadening at about 22°, suggesting the presence of some sp^2-bonded carbons (Fig. 2c). This signal is related to the off-plane X-ray reflection and can be attributed to the turbostratic (amorphous) carbon and graphitic carbon with the sp^2-hybridization, as well as, to carbon atoms with an intermediate sp^2/sp^3 character.

The most significant increase in the width of the first signal at $2\theta = 25.30°$ was observed for non-controlled oxidation using 3 M HNO_3 (Fig. 2a, profile assigned as ox-CNOs), that confirms the structural disorder in their graphitic layers suggesting the most destructive reaction environment.

It correlates well with the observation of these nanostructures using HRTEM (Fig. 1b). The images indicate the discontinuity of more than one graphene layer in the CNO structure and the deformation of the spherical shape, indicating a large structural inhomogeneity manifested by a broad peak. The diffraction broadening is connected with the size of the nanoparticles and formed crystallites and can also be caused by deformations and defects in the crystalline material.

Some XRD profiles show narrow peaks at approximately 18° (Fig. 2b, samples P1 and P11), suggesting the existence of well-ordered domains within the ox-CNOs. We interpret these peaks at $2\theta \approx 18°$ as representing the inter-lattice spacing between the oxidized outer surface layer of the CNOs and the immediately adjacent inner graphene layer. At this angle, the calculated *d*-spacing is about 4.9 Å, which corresponds well to the sum of a typical graphene-graphene interlayer distance (~3.4–3.5 Å) and a single C–O bond (~1.4 Å) linking the oxidized surface layer. It suggests that the oxidation is confined to the outermost shell and does not significantly disrupt the inner graphitic layers. Importantly, these peaks appear only for the two materials prepared by procedures P1 and P11, in which the atomic percent of oxygen-containing groups (such as C–OH, O═C–O–, and Ph–OH) is exceptionally high (77 % and 35 % of the total oxygen content, respectively). In those cases, the outer graphene shell must be both highly organized and uniformly functionalized (via C–O bonds) to give the distinct narrow reflection. HRTEM images of the two samples (Fig. 1c and h) confirm that no significant deformation or interruption of the outer graphene shell is evident, implying that the original ~3.4 Å spacing between graphene layers is preserved during modification. Thus, the outermost carbon atoms modified in P1 and P11 retain high structural coherence. The difference in peak intensity between P1 and P11 further suggests that P11 achieved a higher degree of ordering (see Fig. 1h) and a greater extent of surface C–O functionalization of the CNOs.

Similarly, Pérez-Ojeda et al. showed that reductive potassium intercalation reorganizes the concentric graphitic shells of CNOs, producing staged intercalation compounds with increased interlayer spacings [79]. In p-CNOs, XRD reveals a broad (002) reflection at $d \approx 0.35$ nm, typical of graphitic stacking. Upon potassium intercalation, two distinct periodicities appear at $d \approx 0.76$ nm and $d \approx 0.38$ nm, demonstrating that chemical functionalization promotes ordered shell expansion rather than amorphization [79]. These findings highlight that surface chemistry and structural ordering evolve together: intercalants or covalent addends can selectively expand and organize specific shells while maintaining graphitic registry in the rest of the particle. By analogy, the mid-angle reflection observed near $2\theta \approx 18°$ ($d \approx 4.9$ Å) in ox-CNOs can be attributed to a well-ordered outer oxidized shell separated from the adjacent inner graphene layer by the sum of a C–O bond length and the intrinsic intershell spacing [79]. This feature serves as a structural signature of shell-selective oxidation and ordering in the P1 and P11 samples, analogous to the ordered staging reported for potassium-intercalated CNOs.

Another plausible interpretation of the diffraction signal at $2\theta \approx 18°$ is that it originates from layered or partially ordered graphitic-oxide

frameworks. For example, Bhatti et al. reported a distinct peak at ~18° XRD patterns as indicative of graphite oxide in composite membranes [80]. Specifically, the presence of a peak at ~18° suggests a larger interlayer spacing than pristine graphite (2θ~26.5°, d~3.35 Å) and is consistent with the insertion of functional groups, defects or structural disorder in graphene-derived systems [81]. For instance, studies on graphite oxide and reduced graphene oxide have shown interlayer distances on the order of ~10 Å (2θ~9°) for highly oxidized material, which collapse to ~3.6 Å (2θ~24°) upon reduction [81]. However, wider peaks (and lower 2θ) such as ~18° correspond to intermediate states of graphitic ordering, partially exfoliated stacking, or the presence of turbostratic carbon. In one report of N-doped carbon dots with multi-layered structures, a broad peak centered at 2$\theta \approx 18.5°$ was associated with poor graphitic crystallinity and multi-layered assemblies [82].

Thus, the diffraction feature at 18° in CNOs can be interpreted as evidence of layered CNs, likely a mixture of oxidized graphene-type planes or partly reassembled graphite-like domains. The existence of this peak implies the presence of some degree of crystalline (or quasi-crystalline) ordering. These reports support the interpretation that a narrow reflection at 18° in CNO>O/OH(P1) and CNO—COOH(P11) signals an ordered, shell-selective expansion at the particle surface, here plausibly the sum of a C—O bond length (~1.4 Å) and the native intershell spacing (~3.4–3.5 Å), while inner shells remain largely unperturbed and graphitic (as also suggested by HRTEM). This diffraction data provides insight into the structural coherence, interlayer spacing variation, and layered nano-architectures of the carbon phase in the material, as well as the functionalization of the surface CNOs oxygen-containing groups.

3.3. Determination of surface topology using XPS analysis

The chemical state of C and O elements present on CN's surface was analyzed using X-ray photoelectron spectroscopy (XPS). The analysis of XPS data for the functionalized CNs in the C 1 s and O 1 s regions provides information about the chemical bonds between carbon and oxygen atoms, but also between the carbon atoms themselves, such as sp^2- and sp^3-hybridized carbon and disordered carbon and defective carbon atoms (assigned as DSC) [83–85]. Assessment of the percentage of C atoms from the XPS spectra requires separating it into components representing different chemical forms of carbon that are defined by the binding energy (BE). Comparison of components of C 1 s and O 1 s spectra for p-CNOs with those functionalized CNOs makes it possible to observe the progress of the chemical modifications of the CN's surface that lead to changes in the parameters mentioned above (Fig. 3; Tables 1, S3 and S4). For perfectly HOPG structure, the C 1 s spectrum consists of a single feature centered at 284.5 eV corresponding to sp^2-hybridized C atoms [86,87]. For defective HOPG, additional components appear at lower binding energies associated with the lost C atoms (C vacancies) around the hexagons based on the density functional theory [87].

Two prominent peaks for the NDs assigned as sp^3-hybridized C atoms in C—H and C—C are considered at 285.0 and 285.4 eV, respectively [88,35,33,85]. In carbon nanomaterials, intermediate sp^2 and sp^3 states of C atoms are also present at 285.0 eV and are defined as a disordered carbon [84].

The deconvoluted XPS spectra show one dominant peak for p-CNOs at 284.5 eV (Table 2, Fig. 3a, peak A_c), which is related to the presence of sp^2-hybridized C atoms and their amount in the material is estimated at 84.5 at.%. The percentages of individual C and O atoms, calculated from the deconvoluted XPS spectra of C 1s and O 1s, are summarized in Tables 2, S3 and S4. The presence of sp^3-hybridized C atoms in p-CNOs was also noted at 285.0 eV (C—H sp^3) at 3.9 at.% and 286.5 eV (C—C sp^3) at 4.4 at.%, presented in Fig. 3 as B_c and C_c peaks, respectively. In p-CNOs, defective C atoms are also present at 283.9 eV, about 4.6 at.%. In the p-CNOs sample, the presence of C—O bonds was also noted in quantity 2.6 at.%, related to a small number of O atoms remaining after obtaining p-CNOs from NDs. In the last stage, the sample is annealed at 400 °C in an air atmosphere to remove amorphous carbon from the p-CNOs surface. This value will not be considered further in the discussion about the functionalization of the p-CNOs surface in the oxidation process.

Table 2
Elemental analysis of p-CNOs and ox-CNOs based on XPS studies.

Materials	C (%)	O (%)	Other elements (%)	%sp^2 C1s	%sp^3 C1s	Ratio C1s% sp^2/%sp^3
p-CNO	97.4	2.6	-	84.5	4.4	19.2
CNO>O/OH (P1)	94.6	5.4	-	82.5	4.9	16.8
CNO>O(P2)	89.8	9.2	1.0	76.7	6.0	12.8
CNO>O/OH (P3)	88.3	10.5	1.2	73.7	6.3	11.7
CNO>O/OH (P4)	94.1	5.9	-	81.9	5.3	15.5
CNO>O(P5)	93.8	3.6	2.6	82.0	4.3	19.0
CNO>O/ COOR(P6)	98.1	1.9	-	81.2	4.6	17.7
CNO>O/ COOH(P7)	91.3	8.7	-	82.2	4.4	18.7
CNO>O/ COOH(P8)	84.2	10.2	5.6	83.2	4.4	18.9
CNO>O/OH (P9)	94.9	1.7	3.4	83.3	4.7	17.7
CNO>O/ COOR (P10)	95.4	4.7	-	82.4	5.8	14.2
CNO-COOH (P11)	81.5	13.0	5.5	73.7	6.2	11.9

The C 1s spectra in Fig. 3b and c show that after p-CNOs (Fig. 3a) oxidation processes the sp^2 peak at 284.5 eV undergoes a line shape modification by broadening of the C—C component, that transforms into C—O bonds. Contribution of C—O bonds in the C 1s spectra is confined to the region between sp^3-hybridized C atoms at 286.5 eV and π-π* satellite at approximately 291 eV, which is defined as layer-to-layer interactions and/or topographic effect [84]. In the range from 286.3 eV to 288.8 eV, after deconvolution of the C 1s peak, we identified five different peaks (Fig. 3 and Tables S3 and S4), corresponding to the C–O bonds, indicating the surface modification of the p-CNOs structure using the successive P1–P11 procedures. In this range for HOPG and graphene, characteristic regions can be distinguished for C–O bonds, namely C—O- (285.4–287.0 eV), C–O–C (285.6–286.9 eV), C═O (286.8–288.3 eV) and O═C—OH/O═C—OR (288.0–289.5 eV) [86]. On this basis and after a thorough literature analysis, after deconvolution of XPS C 1s spectra for individual ox-CNOs, we determined the type of functional groups on the p-CNOs surface for nanoparticles modified by the P1-P11 procedures, and the detailed data are summarized in Tables 2, S3 and S4. Deconvolution of XPS spectra of the C 1 s spectral region of p-CNOs and ox-CNOs gives the following assignments: DCS at 283.9 eV; A_C at 284.5 eV (C═C sp^2); B_C at 285.0 eV (C—H sp^3); C_C at 285.6 eV (C—C sp^3 in-plane ether C—O-C); D_C at 286.3 eV (-C-O; -C-OH; epoxy -C-O—C-); E_C at 287.0 eV (ether C—O-C); F_C at 287.5 ± 0.1 eV (C═O); G_C at 288.1 eV (O═C—O-) and H_C at 288.8 0.1 eV (O═C—OH) (Fig. 3).

Analysis of the O 1 s XPS spectra of the ox-CNOs can complete the data obtained by analysis of the C 1 s spectra. Deconvolution of the O 1 s spectra for the ox-CNOs resulted in four peaks located at the range 530.9–534.2 eV and one additional peak at 536.0 ± 0.1 eV, that is assigned to adsorbed water (Fig. 4) [89,90]. Peaks A_O at 530.9 ± 0.4 eV (quinonic C═O), B_O at 531.8 ± 0.4 eV (O═C—O-; ketonic C═O; epoxy C—O-C), C_O at 532.9 ± 0.4 eV (ether-like C—O-C; C—OH), D_O at 534.2 ± 0.6 eV (Ph—OH; O=C—O-) and E_O at 536.0 ± 0.1 eV (adsorbed water) are determined for the ox-CNOs obtained from the deconvolution of the O 1 s spectra by XPS (Fig. 4 and Tables S3 and S4) [91,89,92,93,90]. Quantitative analysis of C—O bonds in p-CNOs oxidized according to procedures P1-P11 allowed us to propose dominant functional groups present on the surface of ox-CNOs (Table 1). Due to the fact that the

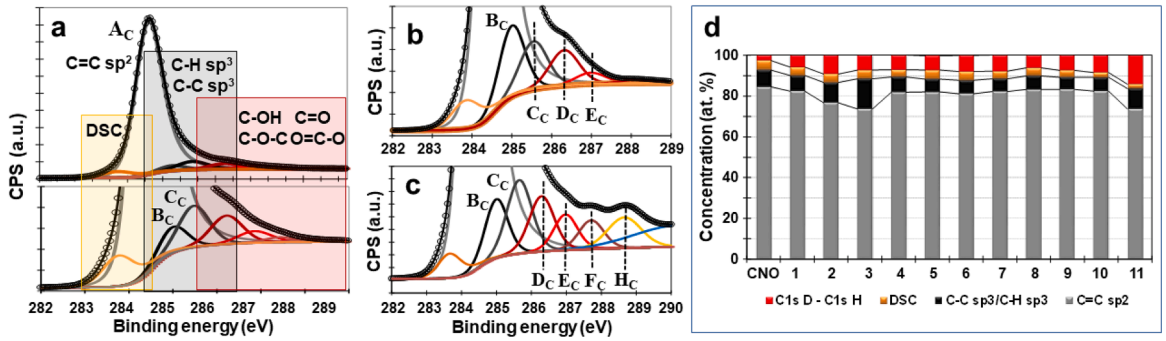

Fig. 3. Deconvolution of XPS spectra of the C 1 s spectral region of (a) p-CNOs; p-CNOs functionalized with the procedure (b) P1 and (c) P11, gives the following assignments: DSC at 283.9 eV; A_C at 284.5 eV (C═C sp^2); B_C at 285.0 eV (C—H sp^3); C_C at 285.6 eV (C—C sp^3 in-plane ether C—O-C); D_C at 286.3 eV (-C-O; -C-OH; epoxy -C-O—C-); E_C at 287.0 eV (ether C—O-C); F_C at 287.5 ± 0.1 eV (C═O); G_C at 288.1 eV (O═C—O-) and H_C at 288.8 0.1 eV (O═C—OH). (d) The analysis of the BE expressed as the concentrations of a chemical state of C for p-CNOs and the functionalized forms of p-CNOs by P1-P11.

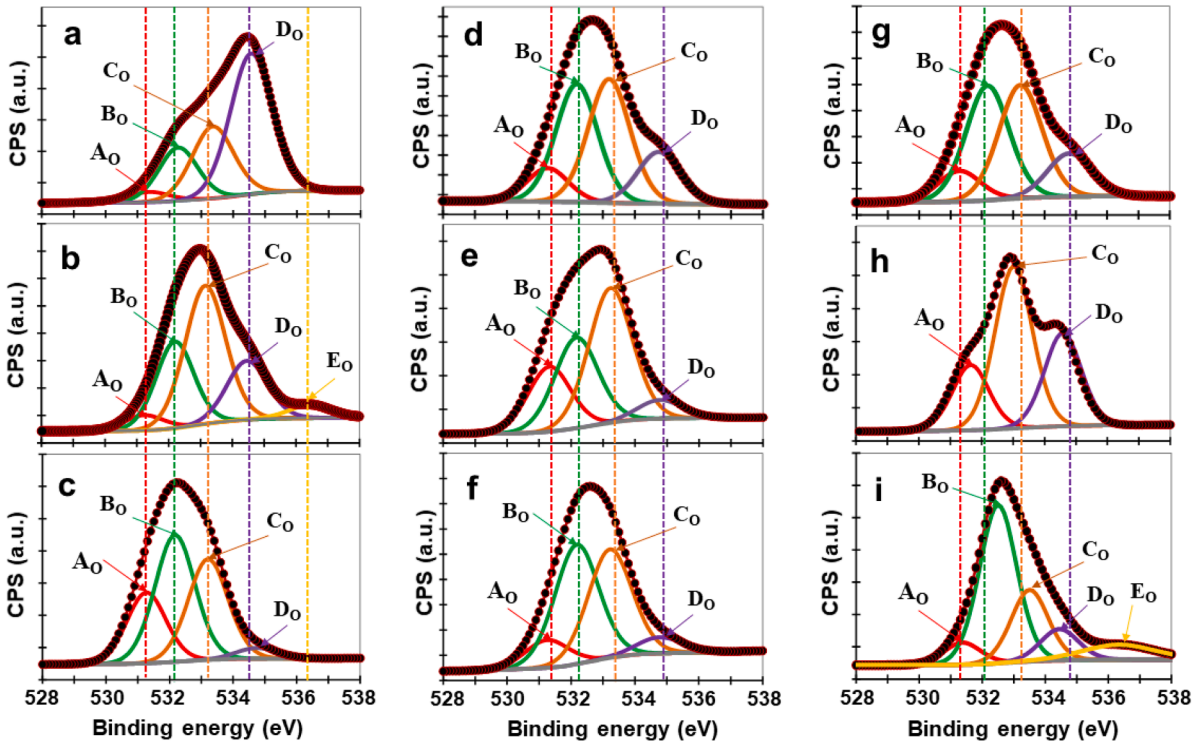

Fig. 4. Deconvolution of XPS spectra of the O 1 s spectral region of p-CNOs functionalized using procedures: (a) P1, (b) P3, (c) P5, (d) P6, (e) P7, (f) P8, (g) P9, (h) P10 and (i) P11. Peaks A_O (quinonic C═O), B_O (O═C—O-; ketonic C═O; epoxy C—O-C), C_O (ether-like C—O-C; C—OH), D_O (Ph-OH; O═C—O-) and E_O (adsorbed water) are determined for the functionalized CNOs obtained from the deconvolution of the O 1 s spectra by XPS.

convolution of XPS C 1s and O 1s spectra gives peaks at a specific BE, for which several functional groups can be assigned (Tables S3 and S4), we performed a simple test of the dispersibility of ox-CNOs in water (Fig. 4). The images shows ox-CNOs divided into two groups, those that even after two months gave very 'well-dispersed' nanoparticles at a concentration of 0.1 mg mL^{-1} in water (Fig. 5b) and those, hereinafter referred to as 'poorly-dispersed', not dispersing at all or in a small amount (Fig. 5a). For comparison, pictures of p-CNOs and oxidized nanoparticles, in the standard procedure using 3 M HNO_3, are also presented. Procedures P1-P3 and P5 are used for the oxidation of p-CNOs, and they give reaction products, the functional groups of which on the surface of functionalized nanostructures are nonpolar, giving CNO>O/OH or CNO>O functionalization. It should therefore be assumed that on the surface of ox-CNOs, C═O groups, which are assigned to quinone, ketonic and aldehyde groups, alcoholic or phenolic, and C—O-C groups of epoxy and ether-like type, dominate. For ox-CNOs oxidized using procedure P4, the XPS O 1s deconvolution spectrum indicates a significant percentage of C—O groups for BE 531.8 eV (44.9 at.%) and 532.9 eV (33.9 at.%) (Table S1). Similarly, for the P9 procedure, for BE, 531.8 eV calculated values 38.0 at.% and 532.9 eV calculated values 37.0 at.%. In this case, the XPS O 1s spectrum deconvolution indicates the presence of a peak at 534.2 eV with a determined percentage content of 14.6 % (Table S4). For both ox-CNOs oxidized using the P4 and P9 procedures, taking into account also the XPS C 1s spectra deconvolution, it can be concluded that in both cases, on the CNOs surface, there are also polar O═C—O- and C—OH/Ph—OH groups, which provide a 'low dispersion' of carbon nanoparticles in water (Fig. 5a).

It should be emphasized here, however, that a significant share of ketonic and aldehyde C—O-C groups and epoxy and ether-like C—O-C groups is noted in both cases. In the case of the procedures P6-P8 and P10 and P11, a 'stable dispersion' of ox-CNOs in water was obtained (Fig. 5b). In all cases, the XPS C 1s and XPS O 1s spectra deconvolution

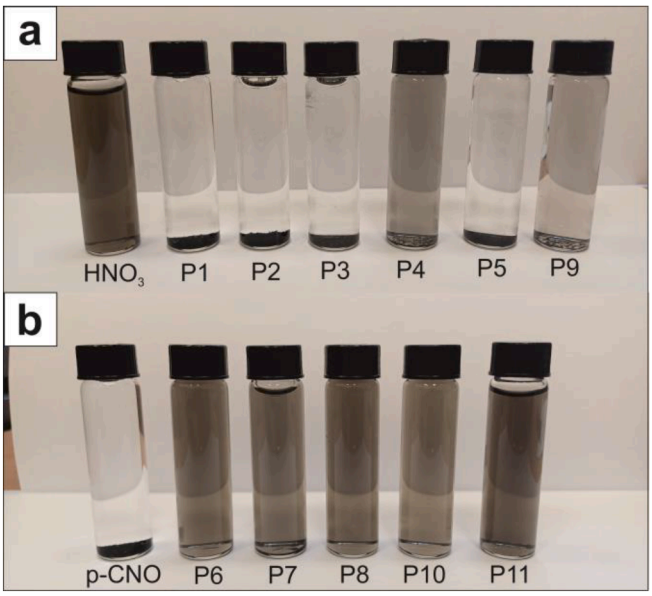

Fig. 5. Images of the (a) poorly- and (b) well-dispersed functionalized p-CNOs in water (after two months, 0.1 mg mL^{-1}). For the comparison, p-CNOs oxidized in (a) 3 M HNO_3 and (b) non-functionalized p-CNOs were presented in water.

indicate a significant amount of polar groups of the O═C—O- and O═C—OH type on the CNOs surface [89,92,93], which ensures their excellent and 'stable' dispersion in water (Fig. 5b, Tables S3 and S4).

For CNOs, the variation of the sp^2 to sp^3 carbon ratio from fitting the C 1s core level was used to confirm the progress of the oxidation reaction of the p-CNOs surface (Table S1 and Fig. 3d) during the chemical treatment of these nanoparticles. For p-CNOs, the sp^2 to sp^3 carbon ratio (expressed in at.%) from fitting the C 1s core level is 19.2 at.%. As a result of the functionalization of the CNO surface, in all cases, a decrease in the value is observed to the minimum values of 11.7 at.% for CNO>O/OH(P3) and 11.9 at.% for CNO—COOH(P11). In each case, as a result of the P1-P11 reaction procedures, the sp^2 to sp^3 hybridized carbon atoms are oxidized, which indicates the progress of the oxidation reaction in all cases. It should be emphasized, however, that the degree of oxidation is expressed as a decrease in the amount of at.% cannot be considered as an absolute degree of functionalization directly influencing the increase in the dispersity of the obtained material. Therefore, the type of functional groups formed on the CNO surface should be carefully considered, as they play a significant role in this process.

For the functionalized CNOs, XPS revealed an increase of the oxygen content from 2.6 at.% for p-CNOs to 13.0 at.% for CNO—COOH(P11), with a simultaneous decrease in sp^2 content at C 1s core level. Only in the case of CNO>O/COOR(P6) was a decrease in the amount of oxygen observed concerning p-CNOs, to a value of 1.9 at.%. However, it should be emphasized that the amount of sp^2-hybridized carbon atoms decreased from a value of 84.5 to 81.2 at.% and the sp^2/sp^3 ratio from 19.2 to 17.7 at.% for p-CNOs and CNO>O/COOR(P6), respectively (Table 2). Additionally, it should be noted that the XPS O 1s deconvolution spectrum (Fig. 4d and Table S3) indicates that for BE at 534.2 eV 16.0 at.% O═C—O- (peak D_o) is assigned; for BE, it is at 531.8 eV 36.1 at.% O═C—O- (peak B_o) is assigned. It indicates many carboxyl-like groups on the ox-CNO surface responsible for the high dispersion of CNO>O/COOR(P6).

Qualitative analysis of XPS O 1s spectra also indicates that the deconvolution spectra for CNO>O/COOR(P10) and CNO—COOH(P11) differ significantly from the other ox-CNOs (Fig. 4, Tables S3 and S4). For CNO>O/COOR(P10), the deconvolution XPS O 1s spectrum indicates the presence of three peaks (Fig. 4h). The first one, characteristic for quinonic groups, is shifted by 0.4 eV (531.3 eV) concerning HOPG and the amount of these atoms is estimated to 20.1 at.% O atoms. The second peak of C_o at 532.9 eV, dominant in the deconvoluted spectra of XPS O 1s, is assigned in this case to a significant amount of ether-like C—O-C groups (50.9 at.%). The last D_o peak, corresponding to O═C—O- bonds, at 534.2 eV, corresponds to the estimated 29 at.% O atoms. On this basis, it was indicated that on the ox-CNOs surface, the decisive groups on the nanoparticle surface are ester groups, which determine the excellent dispersibility of these nanoparticles in water. In turn, for CNO—COOH(P11), the deconvoluted XPS O 1s spectrum indicates the presence of five peaks (Fig. 4i). In this case, the dominant peak is B_o at 531.8 eV, estimated at 53 at.% O (Table S4). In this case, a significant amount of adsorbed water was also noted, the E_o peak at 536.0 eV, in the amount of 5.3 at.% O. The presence of these two peaks allowed us to conclude that, in this case, the ox-CNO surface is modified mainly with carboxylic groups, which enabled the adsorption of water molecules on the surface of CNs due to hydrogen interactions.

3.4. *Spectroscopic evaluation of the surface functionalization of CNOs*

Spectroscopic studies were applied to determine the surface modification of the CNOs (Fig. 6) and progress of the surface functionalization of CNOs by controlling a ratio of the sp^2- to sp^3-hybridized carbon atoms in its nanostructure (Fig. 6). The Fourier transform infrared (FTIR) spectra (Fig. 6a and b) showed that regardless of the chosen oxidation procedure and targeting a specific type of functionalization, hydroxyl, carboxyl, carbonyl, and epoxide groups were present on the outer layer of all modified CNOs. Differences in the intensity of individual bands are, in most cases, insignificant, which indicates a slight dominance of groups of a particular type resulting from the applied modification procedure.

In all the functionalized CNOs in the area of 3600–3000 cm^{-1} a strong broad signal corresponding to the stretching vibrations of the O—H groups was present (Fig. 6a and b) [94,20,13]. In the range 1640–1620 cm^{-1} the bending vibration of hydroxyl groups overlapped by the band from stretching vibrations of C═C (1590 cm^{-1}), that were observed in all spectra and were characterized by different intensity ratios (Fig. 6a and b) [14,13,94]. The symmetric stretching vibration of C═O in deprotonated carboxyl groups at wavenumbers 1390 and 1350 cm^{-1} were present in almost all oxidized materials despite CNO>O(P2) and CNO>O/OH(P3). For CNO>O/OH(P3) and CNO>O/COOR(P6), the out of plane bending vibrations O—H at wavenumbers 670 and 615 cm^{-1} were also noticed, respectively.

In the case of the modification based on carboxylation and acetylation, the primary evidence of CNOs functionalization was the band corresponding to the vibrations of the C═O bond in the recorded spectra. The increase in intensity concerning the signal characteristic of vibrations in the C═C skeleton indicated an increase in the degree of modification of a given structure. On this basis, it can be assumed that CNO>O/COOR(P10) have a much greater number of acetyl groups compared to the number of functional groups on the surface of the modified CNOs (CNO>O/COOR(P6), CNO>O/COOH(P7) and CNO—COOH(P11)).

The dependence of the intensity of the ν C═O and ν C═C signals on the degree of functionalization of the structure is mainly well observed in the case of epoxidized CNOs (CNO>O(P2) and CNO>O/OH(P3)), for which the mentioned bands show similar intensity and overlap. Since the epoxy groups are built into the outermost layer's structure, the vibrations from the CNOs skeleton become stronger so that the bands corresponding to the C═C vibrations become more intense. In addition, the bands observed at 1180 and 1100 cm^{-1} most likely corresponds to asymmetric C—O—C bending vibrations in ether, ester or lactone [95,96]. Interestingly, this signal in the spectra of CNOs, which were also modified to obtain epoxide groups (Fig. 6a, spectra P5 and P9; Fig. 6b, spectrum P8), show a low intensity, which indicate a smaller amount of these groups in the structure of mentioned CNOs. For all materials two less distinct bands were also observed at wavenumbers 1505 and 1450 cm^{-1}, which are associated with hexagonal C—C domains in the CNs [13,

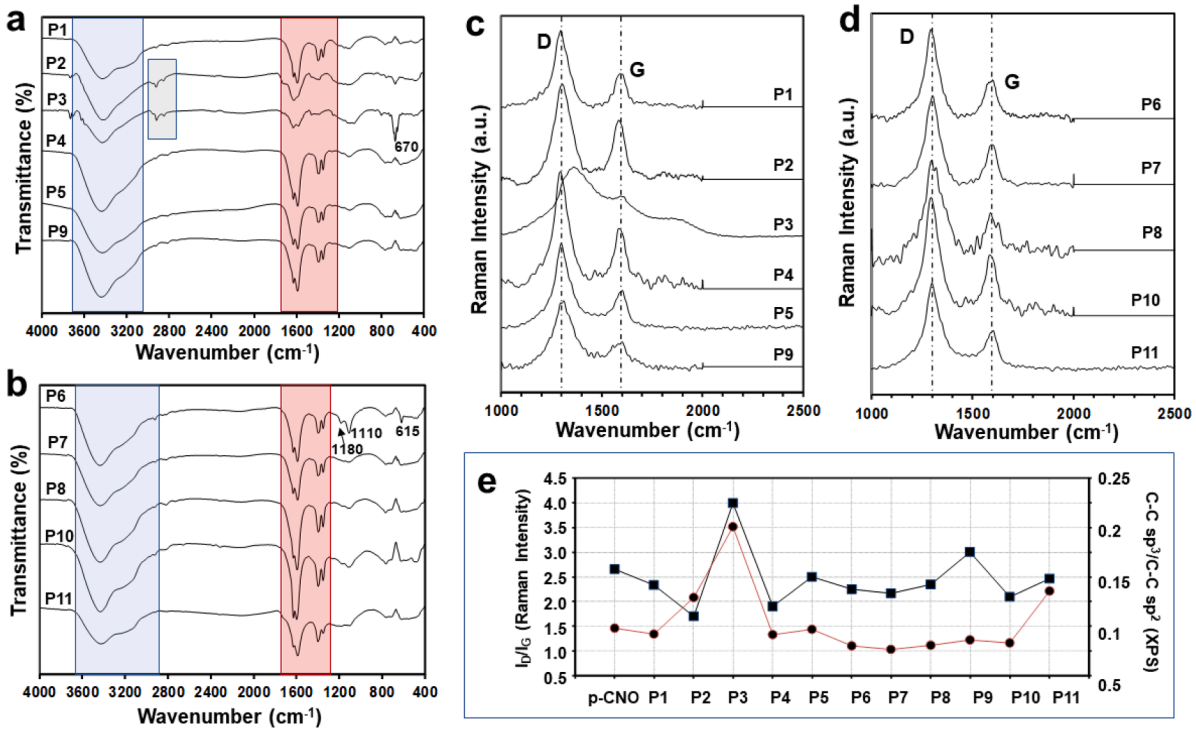

Fig. 6. FTIR spectra of p-CNO oxidized by various procedures from P1 to P11 leading to obtaining (a) poorly- and (b) well-dispersed CNOs in water. Raman spectra of (c) poorly- and (d) well-dispersed CNOs in water. (e) Variation of the I_D/I_G (Raman spectroscopy) and sp^2/sp^3 ratios (XPS studies) for the oxidized CNOs.

97,20].

Raman spectra were recorded for ox-CNOs (Fig. 6a and b), and two characteristic modes were observed for all carbonaceous materials [98]. The band occurring at about 1350 cm^{-1}, the so-called 'D', results from disturbances in the graphite crystal lattice. Defects correspond to vacancies, additional atoms, curvature, and edges [99]. In all spectra, the D-mode was more intense than the G-mode, attributed to sp^2-hybridized carbon atoms and presented in-plane stretching vibrations (E_{2g}). The G-mode in Raman spectra for the highly oriented pyrolytic graphite is observed at 1582 cm^{-1} [100]. It indicates the samples' large share of functional groups and structural defects. For p-CNOs, the D- and G-modes are observed at 1300 and 1590 cm^{-1} (Fig. S1). Along with the G-mode, another weak shoulder is observed near 1610 cm^{-1}, which is assigned as D', that is a disorder-induced in highly-defective graphite [100]. As shown in Figure S1, the D- and G-modes show a broad shape at the base, which sharpens near the maximum. For the G-mode, the doublet structure is caused by the appearance of a distinct shoulder at higher frequencies. This effect is explained by the occurrence of disordered nanocrystalline particles, the existence of different carbon species in the sample (e.g., graphitic nanoribbons) and the tight aggregation of nanoparticles [99,101].

The high inhomogeneity of the material and the increase in size of the nanocrystalline aggregates are evident after surface modification of p-CNO. In Fig. 6c, Raman spectra for poorly-dispersed nanostructures show that the D- and G-modes are weakly formed for CNO>O/OH(P3) due to the numerous epoxy groups observed on the CNO surface. The lack of polar groups on the CNO surface led to the formation of substantial aggregates of nanocrystalline structures. Additionally, it should be emphasized that in the material designated as CNO>O/OH(P3), the presence of a large number of graphitic nanoribbons was observed (Fig. 1d), which confirms the earlier indicated conclusions and observations noted by Zeiger et al., that non-homogenous samples give a picture of poorly developed broad modes D and G [99].

It should also be noted that the D- and G-modes in the Raman spectrum are less developed. For almost all modified CNOs, the D-mode is shifted towards higher wavenumbers by about 10 cm^{-1}. For the G-mode, this difference is even more significant; for CNO—COOH(P11), the value increased by 25 cm^{-1}. This effect was previously observed for ox-CNOs in 6 M nitric acid and suggested a decrease in the diameter of the graphitic nanoparticles with the simultaneous contribution of smaller CNOs in the material [1]. The sp^3 content against the sp^2-hybridized carbon atoms was evaluated based on the areal intensity ratio of I_D/I_G. These values were correlated with the ratio of the percentage of C═C bonds vs. the sum of C—C bonds, C—H bonds and DSC determined based on XPS results. The I_D/I_G ratio decreased due to functionalization relative to the analogous ratio for pristine CNOs for almost all samples. The exceptions are the materials CNO>O/OH(P3) and CNO>O/OH(P9) (Fig. 6e). XPS results were also used to determine the ratio of sp^3 to sp^2 carbon atoms for comparison (Fig. 6e). Also, in this case, the largest share of carbon atoms with sp^3 hybridization was determined for the CNO>O/OH(P3) nanostructure. A significant increase in carbon atoms with sp^3 hybridization was also observed for the CNO—COOH(P11) nanostructure. It proves substantial structural changes in the outermost layer of the modified CNOs. The sp^3/sp^2 intensity ratio value for this nanostructure has a similar trend to that determined by Raman spectroscopy.

3.5. *Determination of surface properties and Hansen solubility parameters of ox-CNOs*

The obtained values of zeta potential for ox-CNOs (Table 3) explain

Table 3
Zeta potential and DLS data for well-dispersible ox-CNOs.

Materials	Zeta potential (mV)	DLS diameters (nm)
CNO>O/COOR(P6)	−42.50 ± 0.18	551.3 ± 101.6
CNO>O/COOH(P7)	−26.11 ± 1.07	217.1 ± 101.0
CNO>O/COOH(P8)	−37.89 ± 1.34	709.8 ± 121.6
CNO>O/COOR(P10)	−39.27 ± 0.26	268.4 ± 128.9
CNO-COOH(P11)	−38.46 ± 1.02	277.8 ± 123.0

the good stability of these functionalized CNOs in water. The zeta potential values are strongly negative, in the range of −26.11 ± 1.07 mV (CNO>O/COOH(P7)) ÷ −42.50 ± 0.18 mV (CNO>O/COOR(P6)), due to the presence of acidic and ester groups on the ox-CNO surface. Obtained hydrodynamic diameters of the ox-CNOs (Table 3) confirm that nanostructures formed nanoaggregates, which confirms their modification, and the small size of the aggregates enables their permanent dispersion in water for a very long time - even up to several months. It should be emphasized, however, that there is no strict correlation between the zeta potential value and the size of nanoaggregates, and based on the obtained results, it cannot be concluded that a lower zeta potential value indicates the formation of smaller nanoaggregates. It is because DLS is a dynamic quantity, and its determination is subject to a significant error of approximately 100 nm. It, as in the case of CNO>O/COOH(P7), is approximately 50 % of the estimated value, 217.1 ± 101.0 nm.

It should be emphasized, however, that the size of aggregates in all tested nanostructures is in the nanometric scale. Assuming that one p-CNO has a diameter of about 5–6 nm, it can be concluded that CNOs oxidized using the P6-P8, P10 and P11 procedures, form aggregates in water, accumulating about 40–120 nanostructures.

Summing up, applied in this study, procedures of CNO modifications have a remarkable influence on the zeta potential as well as on the sizes of CNO aggregates, and this can have a crucial impact on potential applications [1]. The dispersion behaviour of ox-CNOs prepared following procedures P2, P6–8, P10, P11, and oxidation in 3 M HNO_3 was addressed in a series of protic, aprotic polar and nonpolar solvents as described previously for p-CNOs [46]. After ultrasonic treatment of the ox-CNOs/solvent mixture, an arbitrary score of 1 was assigned to solvents where good dispersions were obtained, and 0 to those yielding poor or no dispersions. The criterion for good or bad dispersion was based on visual inspection. The results of the dispersion tests are summarized in Table S5. The HSPs of each tested solvent were obtained from the literature [48]. In all cases, dispersive (δ_D), dipolar (δ_P), hydrogen bond (δ_H) and minimum radius (R_0) values are expressed in $MPa^{0.5}$ units. Each ox-CNOs presented a particular dispersion behaviour corresponding to the different nature and relative proportion of functional moieties on their surfaces as indicated by XPS analysis.

The experimental dispersibility data was then used to determine the HSPs for these ox-CNOs. The HSPs represent the contributions from δ_D, δ_P, and δ_H interactions between two species. Determining these parameters effectively evaluates material solubilities or dispersibilities in different solvents or, in general, the interaction between two substances. The HSPs for ox-CNOs were determined using the algorithm developed by Gharagheizi, which has been successfully employed in previous research to estimate HSPs for polymeric materials [102,103,47]. The algorithm seeks to fit the experimental dispersion data to a sphere with R_0 and the center defined by the δ_D, δ_P, and δ_H for the material, such as that only good solvents lie inside and all bad solvents outside the sphere. This task can be considered an optimization problem and was solved using different global and local solvers implemented in the Optimization Toolbox of MATLAB® version R2018b.

The average values of δ_D, δ_P, δ_H and R_0 for each ox-CNOs are summarized in Table 4, and the reported parameters for p-CNOs. The estimated HSP values reflect some features of the ox-CNOs under study. The small diameter of these CNOs increases the number of π-π interactions between them, which results in the relatively high value of the δ_D term among pristine and ox-CNOs [104]. The δ_P term was also high for most of the ox-CNOs. This term accounts for the dipole moment, which is increased by introducing defects or carbon atoms with sp^3 hybrid orbitals on the structure of these materials [105]. Thus, it might indicate the degree of functionalization of the carbon material.

These values correspond with the XPS analysis that indicated many polar groups of the O═C—O-, O═C—OH, and C—OH/Ph—OH type on the ox-CNOs surface. Moreover, the CNO—COOH(P11) nanoparticles presented the highest δ_P term among the analyzed ox-CNOs. It is clear

Table 4
HSPs for pristine and functionalized CNOs calculated using different optimization algorithms implemented in MATLAB®.

Materials	Parameters			
	δ_D	δ_P	δ_H	R_0
CNO>O(P2)	18.1	9.9	4.3	4.6
CNO>O/COO-(P6)	17.1	10.2	18.0	8.2
CNO>O/COOH(P7)	16.9	9.4	14.8	4.6
CNO>O/ COOH(P8)	18.0	5.2	4.8	3.9
CNO—$COCH_3$/ COOH(P10)	18.9	8.6	18.8	6.9
CNO—COOH(P11)	17.0	15.1	14.3	6.3
CNOs (3 M HNO_3)	18.2	7.2	13.8	6.5
CNO*	15.9	10.0	8.0	8.4

evidence of their high functionalization degree, which is also reflected in a higher percentage (13 %) of oxygen atoms attributed mainly to carboxylic moieties. The similar δ_P value for CNO>O(P2), CNO>O/COO (P6), CNO>O/COOH(P7), and CNO—$COCH_3$/COOH(P10) concerning the reported values for p-CNOs might be a consequence of the presence of a defect and oxygen-containing species on the latter. In the case of the δ_H term, the higher values were obtained for CNO>O/COOR(P6), CNO>O/COOH(P7), CNO—$COCH_3$/COOH(P10), CNO—COOH(P11), and 3 M HNO_3 ox-CNOs. Since this term accounts for the hydrogen-bond interactions, the greater the number of functional groups that form hydrogen bonds, the greater the value of this parameter. Hence, it might be inferred that these materials contain a high number of hydrogen-bonding moieties on their surfaces. The XPS analysis indicated that the surface of these ox-CNOs was mainly functionalized with carboxylic and ester moieties. These functional groups are very effective in forming hydrogen bonds with polar solvents and explain the dispersibility of these nanostructures in water.

A piece of visual evidence that the optimization algorithms were valid to determine the HSPs for ox-CNOs can be obtained by using the estimated HSPs and R_0 values to construct the Hansen solubility sphere (Fig. 7). The Hansen solubility sphere has a radius R_o and a center at δ_D, δ_P, and δ_H.

Fig. 7 shows the Hansen solubility sphere plotted in a three-dimensional space with axes δ_D, δ_P, and δ_H for CNO>O/COOR(P6) and CNO—COOH(P11) nanostructures as a representative example. The good and bad solvents were also plotted in green and red symbols, respectively. It is seen that all 'good solvents' were inside the sphere while most of the 'bad' ones were outside. However, in a few cases, some bad solvents (less than three) laid inside the spheres. These solvents might be considered outliers and might be an expected result due to the limitations of the Hansen approach.

4. Conclusions

Selective oxidation of sp^2-carbon nanostructures enables introduction of targeted surface functionalities. By systematically comparing multiple oxidation routes on CNOs, we identified efficient, condition-matched protocols to deliver predefined functional groups with high dispersibility in polar solvents. Microwave heating provided rapid reaction acceleration. It was determined that substances such as quaternary ammonium salts, acetonitrile and primary tertiary amines behave as co-catalysts hydroxylation and epoxidation reaction of C(sp^2)-hybridized CNs.

For CNOs, the variation of the sp^2 to sp^3 carbon ratio from XPS and Raman spectroscopic studies was used to confirm the progress of the oxidation reaction of the p-CNOs surface during the chemical treatment of these nanoparticles. For p-CNOs, the sp^2 to sp^3 carbon ratio (expressed at.%) from fitting the XPS C 1s core level is 19.2 at.%. In all cases, a decrease in the value is observed to the minimum values of 11.7 at.% for CNO>O/OH(P3) and 11.9 at.% for CNO—COOH(P11). It should be emphasized, however, that not all of the proposed procedures are effective in obtaining CNs with high dispersion in polar solvents.

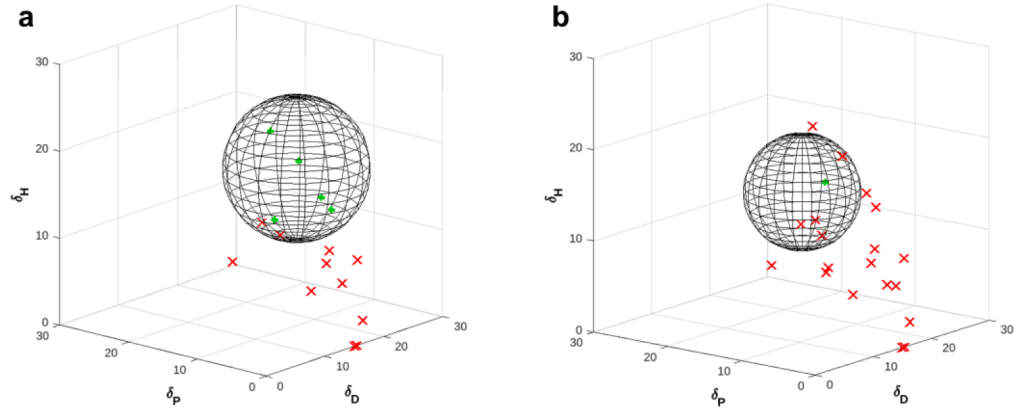

Fig. 7. Hansen solubility sphere for the functionalized CNO calculated with the HSPs and R_0 values in Table 4 (a) CNO>*O*/COO(P6) and (b) CNO—COOH(P11). Green sphere points indicate good solvents and red crosses indicate bad solvents from Table S5.

Using reagents such as urea hydrogen peroxide complex, acetic chloride, acetic anhydride, sodium hypochlorite, and trifluoroacetic acid leads to forming oxygen-containing groups. Those reactions that led to the formation of CNs with carbonyl, ether, epoxy, and phenolic/hydroxyl groups on their surface determined the lack or low dispersion. The most effective functionalization of CNOs, leading to high dispersity of structures, was achieved in the presence of trifluoroacetic acid and/or acetic anhydride. XPS studies confirmed that the ester and carboxyl groups on the surface of CNOs were created due to this modification. Particularly effective is the modification in the presence of sodium hypochlorite, which was used as a subsequent reaction of the two preceding CNO's oxidation reactions, giving CNO>O/COOH(P7) and CNO—COOH(P11) products. On the CNO>O/COOH(P7) surface was found XPS 8.7 at.% and 13 at.% of oxygen on the CNO—COOH(P11) surface, in which carboxyl groups constituted the largest share. The zeta potential values are strongly negative, in the range of -26.11 ± 1.07 mV (CNO>O/COOH(P7)) ÷ -42.50 ± 0.18 mV (CNO>O/COOR(P6)), due to the presence of acidic and ester groups on the CNO surface. Obtained hydrodynamic diameters of the ox-CNOs confirm that nanostructures formed nanoaggregates, which confirms their modification, and the small size of the aggregates enables their permanent dispersion in water for a very long time. The calculated HSP parameters agreed with the nature of the functional groups introduced on the p-CNOs and with the XPS results, revealing their usefulness in estimating the surface properties of carbon nanomaterials and the possibility of predicting their dispersion behaviour in other solvents. Collectively, these advances provide practical guidance for choosing oxidation pathways that balance functional-group introduction with dispersion stability, enabling rational surface design of CNOs for electrochemical, catalytic, and biomedical applications.

CRediT authorship contribution statement

Marta E. Plonska-Brzezinska: Writing – review & editing, Writing – original draft, Visualization, Validation, Supervision, Project administration, Methodology, Investigation, Funding acquisition, Formal analysis, Data curation, Conceptualization. **Joanna Breczko:** Writing – original draft, Methodology, Investigation. **Damian Pawelski:** Methodology, Investigation. **Julio César Zuaznabar Gardona:** Methodology, Investigation. **Alex Fragoso:** Writing – review & editing, Writing – original draft, Methodology, Investigation. **Krzysztof Brzezinski:** Writing – review & editing, Writing – original draft, Methodology, Investigation. **Artur P. Terzyk:** Writing – review & editing, Writing – original draft, Methodology, Investigation.

Declaration of competing interest

The authors declare the following financial interests/personal relationships which may be considered as potential competing interests:

Marta E. Plonska-Brzezinska reports financial support was provided by National Science Centre Poland. None If there are other authors, they declare that they have no known competing financial interests or personal relationships that could have appeared to influence the work reported in this paper.

Supplementary materials

Supplementary material associated with this article can be found, in the online version, at doi:10.1016/j.apsadv.2025.100906.

Data availability

Data will be made available on request.

References

[1] M.A. Lucherelli, L.M.S. Stiegler, F. Steiger, E.H. Åhlgren, J. Requena-Ramírez, E. Castro, L. Echegoyen, A. Hirsch, W. Peukert, J. Kotakoski, J. Walter, M. E. Pérez-Ojeda, G. Abellán, Carbon nano-onions: individualization and enhanced water dispersibility, Carbon 218 (2024) 118760, https://doi.org/10.1016/j.carbon.2023.118760.

[2] V. Datsyuk, M. Kalyva, K. Papagelis, J. Parthenios, D. Tasis, A. Siokou, I. Kallitsis, C. Galiotis, Chemical oxidation of multiwalled carbon nanotubes, Carbon 46 (2008) 833–840, https://doi.org/10.1016/j.carbon.2008.02.012.

[3] D. Stéfani, A.J. Paula, B.G. Vaz, R.A. Silva, N.F. Andrade, G.Z. Justo, C. V. Ferreira, A.G.S. Filho, M.N. Eberlin, O.L. Alves, Structural and proactive safety aspects of oxidation debris from multiwalled carbon nanotubes, J. Hazard. Mater. 189 (2011) 391–396, https://doi.org/10.1016/j.jhazmat.2011.02.050.

[4] H. Yu, Y. Jin, F. Peng, H. Wang, J. Yang, Kinetically controlled side-wall functionalization of carbon nanotubes by nitric acid oxidation, J. Phys. Chem. C 112 (2008) 6758–6763, https://doi.org/10.1021/jp711975a.

[5] A. Chou, T. Böcking, R. Liu, N.K. Singh, G. Moran, J.J. Gooding, Effect of dialysis on the electrochemical properties of acid-oxidized single-walled carbon nanotubes, J. Phys. Chem. C 112 (2008) 14131–14138, https://doi.org/10.1021/jp7113785.

[6] J. Zhang, H. Zou, Q. Qing, Y. Yang, Q. Li, Z. Liu, X. Guo, Z. Du, Effect of chemical oxidation on the structure of single-walled carbon nanotubes, J. Phys. Chem. B 107 (2003) 3712–3718, https://doi.org/10.1021/jp027500u.

[7] G. Ning, X. Ma, X. Zhu, Y. Cao, Y. Sun, C. Qi, Z. Fan, Y. Li, X. Zhang, X. Lan, J. Gao, Enhancing the Li storage capacity and initial coulombic efficiency for porous carbons by sulfur doping, ACS Appl. Mater. Interfaces 6 (2014) 15950–15958, https://doi.org/10.1021/am503716k.

[8] X. Li, B. Azimzadeh, C.E. Martinez, M.B. McBride, Pb mineral precipitation in solutions of sulfate, carbonate and phosphate: measured and modeled Pb solubility and Pb2+ activity, Minerals 11 (2021) 620, https://doi.org/10.3390/min11060620.

[9] M. Li, M. Boggs, T.P. Beebe, C.P. Huang, Oxidation of single-walled carbon nanotubes in dilute aqueous solutions by ozone as affected by ultrasound, Carbon 46 (2008) 466–475, https://doi.org/10.1016/j.carbon.2007.12.012.

[10] S. Osswald, M. Havel, Y. Gogotsi, Monitoring oxidation of multiwalled carbon nanotubes by Raman spectroscopy, J. Raman Spectrosc. 38 (2007) 728–736, https://doi.org/10.1002/jrs.1686.

[11] O. Martín, H.R. Gutierrez, A. Maroto-Valiente, M. Terrones, T. Blanco, J. Baselga, An efficient method for the carboxylation of few-wall carbon nanotubes with little damage to their sidewalls, Mater. Chem. Phys. 140 (2013) 499–507, https://doi.org/10.1016/j.matchemphys.2013.03.060.

[12] Y. Miyata, Y. Maniwa, H. Kataura, Selective oxidation of semiconducting single-wall carbon nanotubes by hydrogen peroxide, J. Phys. Chem. B 110 (2006) 25–29, https://doi.org/10.1021/jp055692y.

[13] M.E. Plonska-Brzezinska, A. Lapinski, A.Z. Wilczewska, A.T. Dubis, A. Villalta-Cerdas, K. Winkler, L. Echegoyen, The synthesis and characterization of carbon nano-onions produced by solution ozonolysis, Carbon 49 (2011) 5079–5089, https://doi.org/10.1016/j.carbon.2011.07.027.

[14] J. Ackermann, A. Krueger, Efficient surface functionalization of detonation nanodiamond using ozone under ambient conditions, Nanoscale 11 (2019) 8012–8019, https://doi.org/10.1039/C9NR01716J.

[15] K.J. Ziegler, Z. Gu, J. Shaver, Z. Chen, E.L. Flor, D.J. Schmidt, C. Chan, R. H. Hauge, R.E. Smalley, Cutting single-walled carbon nanotubes, Nanotechnology 16 (2005) S539–S544, https://doi.org/10.1088/0957-4484/16/7/031.

[16] C.-M. Liu, H.-B. Cao, Y.-P. Li, H.-B. Xu, Y. Zhang, The effect of electrolytic oxidation on the electrochemical properties of multi-walled carbon nanotubes, Carbon 44 (2006) 2919–2924, https://doi.org/10.1016/j.carbon.2006.05.046.

[17] Y. Xing, L. Li, C.C. Chusuei, R.V. Hull, Sonochemical oxidation of multiwalled carbon nanotubes, Langmuir 21 (2005) 4185–4190, https://doi.org/10.1021/la047268e.

[18] D.-Q. Yang, E. Sacher, Strongly enhanced interaction between evaporated Pt nanoparticles and functionalized multiwalled carbon nanotubes via plasma surface modifications: effects of physical and chemical defects, J. Phys. Chem. C 112 (2008) 4075–4082, https://doi.org/10.1021/jp076531s.

[19] N.P. Zschoerper, V. Katzenmaier, U. Vohrer, M. Haupt, C. Oehr, T. Hirth, Analytical investigation of the composition of plasma-induced functional groups on carbon nanotube sheets, Carbon 47 (2009) 2174–2185, https://doi.org/10.1016/j.carbon.2009.03.059.

[20] M.E. Plonska-Brzezinska, A.T. Dubis, A. Lapinski, A. Villalta-Cerdas, L. Echegoyen, Electrochemical properties of oxidized carbon nano-onions: DRIFTS-FTIR and raman spectroscopic analyses, ChemPhysChem 12 (2011) 2659–2668, https://doi.org/10.1002/cphc.201100198.

[21] D.M. Bobrowska, P. Olejnika, L. Echegoyen, M. Brzezinska, Onion-like carbon nanostructures: an overview of bio-applications, Curr. Med. Chem. 25 (2018), https://doi.org/10.2174/0929867325666181101105535.

[22] M.E. Plonska-Brzezinska, Carbon nano-onions: a review of recent progress in synthesis and applications, ChemNanoMat 5 (2019) 568–580, https://doi.org/10.1002/cnma.201800583.

[23] J. Bartelmess, S. Giordani, Carbon nano-onions (multi-layer fullerenes): chemistry and applications, Beilstein J. Nanotechnol. 5 (2014) 1980–1998, https://doi.org/10.3762/bjnano.5.207.

[24] V.L. Kuznetsov, A.L. Chuvilin, Y.V. Butenko, I.Y. Mal'kov, V.M. Titov, Onion-like carbon from ultra-disperse diamond, Chem. Phys. Lett. 222 (1994) 343–348, https://doi.org/10.1016/0009-2614(94)87072-1.

[25] A. Palkar, F. Melin, C.M. Cardona, B. Elliott, A.K. Naskar, D.D. Edie, A. Kumbhar, L. Echegoyen, Reactivity differences between carbon nano onions (CNOs) prepared by different methods, Chem. – Asian J. 2 (2007) 625–633, https://doi.org/10.1002/asia.200600426.

[26] K.D. Sattler (Ed.), Carbon Nanomaterials sourcebook. Graphene, fullerenes, nanotubes, and Nanodiamonds, Taylor & Francis Group, Boca Raton, 2016.

[27] A. Hirsch, Principles of Fullerene Reactivity, Fuller. Relat. Struct., 1999, pp. 1–65.

[28] M. Zeiger, N. Jäckel, V.N. Mochalin, V. Presser, Review: carbon onions for electrochemical energy storage, J. Mater. Chem. A 4 (2016) 3172–3196, https://doi.org/10.1039/C5TA08295A.

[29] E. Grądzka, K. Winkler, M. Borowska, M.E. Plonska-Brzezinska, L. Echegoyen, Comparison of the electrochemical properties of thin films of MWCNTs/C60-Pd, SWCNTs/C60-Pd and ox-CNOs/C60-Pd, Electrochim. Acta 96 (2013) 274–284, https://doi.org/10.1016/j.electacta.2013.02.035.

[30] O. Mykhailiv, A. Lapinski, A. Molina-Ontoria, E. Regulska, L. Echegoyen, A. T. Dubis, M.E. Plonska-Brzezinska, Influence of the synthetic conditions on the structural and electrochemical properties of carbon nano-onions, ChemPhysChem 16 (2015) 2182–2191, https://doi.org/10.1002/cphc.201500061.

[31] M.E. Plonska-Brzezinska, A. Molina-Ontoria, L. Echegoyen, Post-modification by low-temperature annealing of carbon nano-onions in the presence of carbohydrates, Carbon 67 (2014) 304–317, https://doi.org/10.1016/j.carbon.2013.09.093.

[32] G.S. Szymanski, Y. Suzuki, T. Ohba, B. Sulikowski, K. Góra-Marek, K.A. Tarach, S. Koter, P. Kowalczyk, A. Ilnicka, M. Zięba, L. Echegoyen, A.P. Terzyk, M. E. Plonska-Brzezinska, Linking the defective structure of boron-doped carbon nano-onions with their catalytic properties: experimental and theoretical studies, ACS Appl. Mater. Interfaces 13 (2021) 51628–51642, https://doi.org/10.1021/acsami.1c12126.

[33] D. Pawelski, O.F. Delgado, A.Z. Wilczewska, J.W. Strawa, M.E. Plonska-Brzezinska, Nanostructured carbon catalyst for amide coupling reactions under microwave heating in the absence of a solvent, ACS Appl. Nano Mater. 5 (2022) 16376–16387, https://doi.org/10.1021/acsanm.2c03437.

[34] H. Asati, R. Mondal, K.M. Tripathi, Ultra-fast microwave catalytic degradation of multiple dyes by waste derived carbon nano onions, Mater. Today Sustain. 26 (2024) 100724, https://doi.org/10.1016/j.mtsust.2024.100724.

[35] O. Mykhailiv, H. Zubyk, K. Brzezinski, M. Gras, G. Lota, M. Gniadek, E. Romero, L. Echegoyen, M.E. Plonska-Brzezinska, Improvement of the structural and chemical properties of carbon nano-onions for electrocatalysis, ChemNanoMat 3 (2017) 583–590, https://doi.org/10.1002/cnma.201700161.

[36] G.S. Szymański, M. Wiśniewski, P. Olejnik, S. Koter, E. Castro, L. Echegoyen, A. P. Terzyk, M.E. Plonska-Brzezinska, Correlation between the catalytic and electrocatalytic properties of nitrogen-doped carbon nanoonions and the polarity of the carbon surface: experimental and theoretical investigations, Carbon 151 (2019) 120–129, https://doi.org/10.1016/j.carbon.2019.05.069.

[37] O. Butsyk, P. Olejnik, E. Romero, M.E. Plonska-Brzezinska, Postsynthetic treatment of carbon nano-onions: surface modification by heteroatoms to enhance their capacitive and electrocatalytic properties, Carbon 147 (2019) 90–104, https://doi.org/10.1016/j.carbon.2019.02.063.

[38] M.E. Plonska-Brzezinska, D.M. Brus, J. Breczko, L. Echegoyen, Carbon nano-onions and biocompatible polymers for flavonoid incorporation, Chem. - Eur. J. 19 (2013) 5019–5024, https://doi.org/10.1002/chem.201300009.

[39] D.M. Bobrowska, J. Czyrko, K. Brzezinski, L. Echegoyen, M.E. Plonska-Brzezinska, Carbon nano-onion composites: physicochemical characteristics and biological activity, Fuller. Nanotub. Carbon Nanostruct. (2016) 0, https://doi.org/10.1080/1536383X.2016.1248758.

[40] E. Sohouli, M. Ghalkhani, T. Zargar, Y. Joseph, M. Rahimi-Nasrabadi, F. Ahmadi, M.E. Plonska-Brzezinska, H. Ehrlich, A new electrochemical aptasensor based on gold/nitrogen-doped carbon nano-onions for the detection of Staphylococcus aureus, Electrochim. Acta 403 (2022) 139633, https://doi.org/10.1016/j.electacta.2021.139633.

[41] J.-P. Tessonnier, D. Rosenthal, T.W. Hansen, C. Hess, M.E. Schuster, R. Blume, F. Girgsdies, N. Pfänder, O. Timpe, D.S. Su, R. Schlögl, Analysis of the structure and chemical properties of some commercial carbon nanostructures, Carbon 47 (2009) 1779–1798, https://doi.org/10.1016/j.carbon.2009.02.032.

[42] F. Cardona, M. Bonanni, G. Soldaini, A. Goti, One-pot synthesis of nitrones from primary amines and aldehydes catalyzed by methyltrioxorhenium, ChemSusChem 1 (2008) 327–332, https://doi.org/10.1002/cssc.200700156.

[43] F. Okabe-Nakahara, H. Nagabuchi, E. Masumoto, H. Maruoka, Synthesis of benzimidazoles, benzoxazoles and benzothiazole by the reaction of 2-amino-4,5-dihydro-3-furancarbonitrile and o-substituted anilines in the catalysis of trimetylamine hydrochloride, Heterocycles 102 (2021) 2207, https://doi.org/10.3987/COM-21-14529.

[44] D.G. Crosby, E. Leitis, Photodecomposition of chlorobenzoic acids, J. Agric. Food Chem. 17 (1969) 1033–1035, https://doi.org/10.1021/jf60165a011.

[45] G.A. Razuvaev Institute of Organometallic Chemistry of the RAS, Nizhny Novgorod, Russia, V. Semenov, N. Zolotareva, M. Lopatin, Optical properties of triethylaminium salt of trifluoroacetic acid, Bull. South Ural State Univ. Ser. Chem. 16 (2024) 121–126, https://doi.org/10.14529/chem240214.

[46] J.C. Zuaznabar-Gardona, A. Fragoso, Determination of the Hansen solubility parameters of carbon nano-onions and prediction of their dispersibility in organic solvents, J. Mol. Liq. 294 (2019) 111646, https://doi.org/10.1016/j.molliq.2019.111646.

[47] F. Gharagheizi, New procedure to calculate the Hansen solubility parameters of polymers, J. Appl. Polym. Sci. 103 (2007) 31–36, https://doi.org/10.1002/app.23874.

[48] C.M. Hansen, Hansen Solubility Parameters: A User's Handbook, 2nd Edition, 0 ed., CRC Press, 2007 https://doi.org/10.1201/9781420006834.

[49] A. Hirsch, The Chemistry of the Fullerenes, 1. Auflage, Wiley-VCH, Weinheim, 2008.

[50] R.W. Murray, K. Iyanar, Oxidation of [60]fullerene by the methyltrioxorhenium-hydrogen peroxide system, Tetrahedron Lett. 38 (1997) 335–338, https://doi.org/10.1016/S0040-4039(96)02345-3.

[51] K. Kokubo, K. Matsubayashi, H. Tategaki, H. Takada, T. Oshima, Facile synthesis of highly water-soluble fullerenes more than half-covered by hydroxyl groups, ACS Nano 2 (2008) 327–333, https://doi.org/10.1021/nn700151z.

[52] L.Y. Chiang, J.W. Swirczewski, C.S. Hsu, S.K. Chowdhury, S. Cameron, K. Creegan, Multi-hydroxy additions onto C60 fullerene molecules, J. Chem. Soc. Chem. Commun. (1992) 1791, https://doi.org/10.1039/c39920001791.

[53] L.Y. Chiang, R.B. Upasani, J.W. Swirczewski, Versatile nitronium chemistry for C60 fullerene functionalization, J. Am. Chem. Soc. 114 (1992) 10154–10157, https://doi.org/10.1021/ja00052a010.

[54] J. Li, A. Takeuchi, M. Ozawa, X. Li, K. Saigo, K. Kitazawa, C60 fullerol formation catalysed by quaternary ammonium hydroxides, J. Chem. Soc. Chem. Commun. (1993) 1784, https://doi.org/10.1039/c39930001784.

[55] L.Y. Chiang, L.-Y. Wang, J.W. Swirczewski, S. Soled, S. Cameron, Efficient synthesis of polyhydroxylated fullerene derivatives via hydrolysis of polycyclosulfated precursors, J. Org. Chem. 59 (1994) 3960–3968, https://doi.org/10.1021/jo00093a030.

[56] V. Vacque, N. Dupuy, B. Sombret, J.P. Huvenne, P. Legrand, In situ quantitative and kinetic study by Fourier transform Raman spectroscopy of reaction between nitriles and hydroperoxides, J. Mol. Struct. 410–411 (1997) 555–558, https://doi.org/10.1016/S0022-2860(96)09518-X.

[57] G. Laus, Kinetics of acetonitrile-assisted oxidation of tertiary amines by hydrogen peroxide, J. Chem. Soc. Perkin Trans. 2 (2001) 864–868, https://doi.org/10.1039/b102066h.

[58] S. Schrader, E.V. Dehmlow, Hydrogen peroxide and air AS inexpensive oxidants in phase-transfer catalysis. A review, Org. Prep. Proced. Int. 32 (2000) 123–152, https://doi.org/10.1080/00304940009356279.

[59] R.M. Laird, R.E. Parker, The mechanism of epoxide reactions. Part XII. Reactions of ethylene oxide with alcohols in the presence of sodium alkoxides and of

tertiary amines, J. Chem. Soc. B Phys. Org. (1969) 1062, https://doi.org/10.1039/j29690001062.
[60] J.L. Han, K.H. Hsieh, W.Y. Chiu, Kinetics of curing reaction of epoxide catalyzed by tertiary amine, J. Appl. Polym. Sci. 50 (1993) 1099–1106, https://doi.org/10.1002/app.1993.070500618.
[61] S.A. Savage, G.S. Jones, S. Kolotuchin, S.A. Ramrattan, T. Vu, R.E. Waltermire, Preparation of Saxagliptin, a novel DPP-IV inhibitor, Org. Process Res. Dev. 13 (2009) 1169–1176, https://doi.org/10.1021/op900226j.
[62] S. Yamada, T. Mrozek, T. Rager, J. Owens, J. Rangel, C.G. Willson, J. Byers, Toward environmentally friendly photolithographic materials: a new class of water-soluble photoresists, Macromolecules 37 (2004) 377–384, https://doi.org/10.1021/ma034461r.
[63] M.M. Bio, J.L. Leighton, An approach to the synthesis of the phomoidrides, J. Org. Chem. 68 (2003) 1693–1700, https://doi.org/10.1021/jo026478y.
[64] M.-L. Wang, C.-C. Ou, J.-J. Jwo, Effect of organic solvents on the pyridine 1-oxide-catalyzed reaction of benzoyl chloride and acetate ion in a two-phase medium, Ind. Eng. Chem. Res. 33 (1994) 2034–2039, https://doi.org/10.1021/ie00033a003.
[65] S.K. Mohamed, M.A.-M. Gomaa, A.M. Nour El-Din, Reaction of triazene 1-oxides: novel synthesis of solid arenediazonium chlorides†, J. Chem. Res. (1997) 166–167, https://doi.org/10.1039/a605013a.
[66] Y.V. Butenko, V.L. Kuznetsov, A.L. Chuvilin, V.N. Kolomiichuk, S.V. Stankus, R. A. Khairulin, B. Segall, Kinetics of the graphitization of dispersed diamonds at "low" temperatures, J. Appl. Phys. 88 (2000) 4380, https://doi.org/10.1063/1.1289791.
[67] S. Tomita, A. Burian, J.C. Dore, D. LeBolloch, M. Fujii, S. Hayashi, Diamond nanoparticles to carbon onions transformation: X-ray diffraction studies, Carbon 40 (2002) 1469–1474, https://doi.org/10.1016/S0008-6223(01)00311-6.
[68] S. Tomita, M. Fujii, S. Hayashi, K. Yamamoto, Transformation of carbon onions to diamond by low-temperature heat treatment in air, Diam. Relat. Mater. 9 (2000) 856–860, https://doi.org/10.1016/S0925-9635(99)00217-4.
[69] H.W. Kroto, Carbon onions introduce new flavour to fullerene studies, Nature 359 (1992) 670–671, https://doi.org/10.1038/359670a0.
[70] A. Hirsch (Ed.), The Chemistry of the Fullerenes, 1st ed., Wiley, 1994 https://doi.org/10.1002/9783527619214.
[71] V. Pérez-Luna, M. Cisneros, C. Bittencourt, I. Saucedo-Orozco, M. Quintana, Imaging carbon nanostructures' reactivity: a complementary strategy to define chemical structure, R. Soc. Open Sci. 5 (2018) 180605, https://doi.org/10.1098/rsos.180605.
[72] R. Singh, M. Frenklach, A mechanistic study of the influence of graphene curvature on the rate of high-temperature oxidation by molecular oxygen, Carbon 101 (2016) 203–212, https://doi.org/10.1016/j.carbon.2016.01.090.
[73] V.L. Kuznetsov, Y.V. Butenko, V.I. Zaikovskii, A.L. Chuvilin, Carbon redistribution processes in nanocarbons, Carbon N Y 42 (2004) 1057–1061, https://doi.org/10.1016/j.carbon.2003.12.059.
[74] I.V. Ponomareva, L.A. Chernozatonskii, How can carbon onion transform into diamond-like structure, Microelectron. Eng. 69 (2003) 625–628, https://doi.org/10.1016/S0167-9317(03)00354-X.
[75] R.I. Singh, A.M. Mebel, M. Frenklach, Oxidation of graphene-edge six- and five-member rings by molecular oxygen, J. Phys. Chem. A 119 (2015) 7528–7547, https://doi.org/10.1021/acs.jpca.5b00868.
[76] Y. Liu, Y. Zhang, L. Wang, X. Zan, L. Zhang, The role of iodine catalyst in the synthesis of 22-carbon tricarboxylic acid and its ester: a case study, Catalysts 9 (2019) 972, https://doi.org/10.3390/catal9120972.
[77] S. Khanniche, F. Louis, L. Cantrel, I. Černušák, Thermochemistry of HIO_2 species and reactivity of iodous acid with OH radical: a computational study, ACS Earth Space Chem. 1 (2017) 39–49, https://doi.org/10.1021/acsearthspacechem.6b00010.
[78] A.V. Siklitskaya, S.G. Yastrebov, R. Smith, An interpretation of the strongest X-ray diffraction peak for various carbon nanoclusters, Nanosyst. Phys. Chem. Math. (2016) 340–348, https://doi.org/10.17586/2220-8054-2016-7-2-340-348.
[79] M.E. Pérez-Ojeda, E. Castro, C. Kröckel, M.A. Lucherelli, U. Ludacka, J. Kotakoski, K. Werbach, H. Peterlik, M. Melle-Franco, J.C. Chacón-Torres, F. Hauke, L. Echegoyen, A. Hirsch, G. Abellán, Carbon nano-onions: potassium intercalation and reductive covalent functionalization, J. Am. Chem. Soc. 143 (2021) 18997–19007, https://doi.org/10.1021/jacs.1c07604.
[80] H.T. Bhatti, N.M. Ahmad, M.B. Khan Niazi, M.A. Ur Rehman Alvi, N. Ahmad, M. N. Anwar, W. Cheema, S. Tariq, M. Batool, Z. Aman, H.A. Janjua, A.L. Khan, A. U. Khan, Graphene oxide-PES-based mixed matrix membranes for controllable antibacterial activity against *Salmonella typhi* and water treatment, Int. J. Polym. Sci. 2018 (2018) 1–12, https://doi.org/10.1155/2018/7842148.
[81] J. Jagiełło, A. Chlanda, M. Baran, M. Gwiazda, L. Lipińska, Synthesis and characterization of graphene oxide and reduced graphene oxide composites with inorganic nanoparticles for biomedical applications, Nanomaterials 10 (2020) 1846, https://doi.org/10.3390/nano10091846.
[82] F. Du, J. Yuan, M. Zhang, J. Li, Z. Zhou, Z. Li, M. Cao, J. Chen, L. Zhang, X. Liu, A. Gong, W. Xu, Q. Shao, Nitrogen-doped carbon dots with heterogeneous multi-layered structures, RSC Adv. 4 (2014) 37536, https://doi.org/10.1039/C4RA06818A.
[83] B. Lesiak, L. Kövér, J. Tóth, J. Zemek, P. Jiricek, A. Kromka, N. Rangam, C sp2/sp3 hybridisations in carbon nanomaterials – XPS and (X)AES study, Appl. Surf. Sci. 452 (2018) 223–231, https://doi.org/10.1016/j.apsusc.2018.04.269.
[84] R. Blume, D. Rosenthal, J.-P. Tessonnier, H. Li, A. Knop-Gericke, R. Schlögl, Characterizing graphitic carbon with X-ray photoelectron spectroscopy: a step-by-step approach, ChemCatChem 7 (2015) 2871–2881, https://doi.org/10.1002/cctc.201500344.
[85] J.C. Arnault, X-ray photoemission spectroscopy applied to nanodiamonds: from surface chemistry to in situ reactivity, Diam. Relat. Mater. 84 (2018) 157–168, https://doi.org/10.1016/j.diamond.2018.03.015.
[86] X. Chen, X. Wang, D. Fang, A review on C1s XPS-spectra for some kinds of carbon materials, Fuller. Nanotub. Carbon Nanostruct. 28 (2020) 1048–1058, https://doi.org/10.1080/1536383X.2020.1794851.
[87] A. Barinov, O.B. Malcioğlu, S. Fabris, T. Sun, L. Gregoratti, M. Dalmiglio, M. Kiskinova, Initial stages of oxidation on graphitic surfaces: photoemission study and density functional theory calculations, J. Phys. Chem. C 113 (2009) 9009–9013, https://doi.org/10.1021/jp902051d.
[88] M. Koinuma, H. Tateishi, K. Hatakeyama, S. Miyamoto, C. Ogata, A. Funatsu, T. Taniguchi, Y. Matsumoto, Analysis of reduced graphene oxides by X-ray photoelectron spectroscopy and electrochemical capacitance, Chem. Lett. 42 (2013) 924–926, https://doi.org/10.1246/cl.130152.
[89] Y.J. Oh, J.J. Yoo, Y.I. Kim, J.K. Yoon, H.N. Yoon, J.-H. Kim, S.B. Park, Oxygen functional groups and electrochemical capacitive behavior of incompletely reduced graphene oxides as a thin-film electrode of supercapacitor, Electrochim. Acta 116 (2014) 118–128, https://doi.org/10.1016/j.electacta.2013.11.040.
[90] L. Stobinski, B. Lesiak, A. Malolepszy, M. Mazurkiewicz, B. Mierzwa, J. Zemek, P. Jiricek, I. Bieloshapka, Graphene oxide and reduced graphene oxide studied by the XRD, TEM and electron spectroscopy methods, J. Electron Spectrosc. Relat. Phenom. 195 (2014) 145–154, https://doi.org/10.1016/j.elspec.2014.07.003.
[91] R. Larciprete, S. Gardonio, L. Petaccia, S. Lizzit, Atomic oxygen functionalization of double walled C nanotubes, Carbon 47 (2009) 2579–2589, https://doi.org/10.1016/j.carbon.2009.05.008.
[92] R. Larciprete, P. Lacovig, S. Gardonio, A. Baraldi, S. Lizzit, Atomic oxygen on graphite: chemical characterization and thermal reduction, J. Phys. Chem. C 116 (2012) 9900–9908, https://doi.org/10.1021/jp2098153.
[93] H. Zhao, J. Ye, W. Song, D. Zhao, M. Kang, H. Shen, Z. Li, Insights into the surface oxygen functional group-driven fast and stable sodium adsorption on carbon, ACS Appl. Mater. Interfaces 12 (2020) 6991–7000, https://doi.org/10.1021/acsami.9b11627.
[94] M.K. Sreeramoju, J.P. Selegue, R. Podila, A.M. Rao, Surface functional group investigation of oxidized, nanodiamond-derived carbon nano-onions, Mater. Today Commun. 26 (2021) 101966, https://doi.org/10.1016/j.mtcomm.2020.101966.
[95] B.C. Smith, The infrared spectra of polymers V: epoxies, Spectroscopy (2022) 17–19, https://doi.org/10.56530/spectroscopy.mg2473z4.
[96] T. Petit, L. Puskar, FTIR spectroscopy of nanodiamonds: methods and interpretation, Diam. Relat. Mater. 89 (2018) 52–66, https://doi.org/10.1016/j.diamond.2018.08.005.
[97] M.I. Baraton, T. Merle, P. Quintard, V. Lorenzelli, Surface activity of a boron nitride powder: a vibrational study, Langmuir 9 (1993) 1486–1491, https://doi.org/10.1021/la00030a011.
[98] Y. Dong, S. Zhang, X. Du, S. Hong, S. Zhao, Y. Chen, X. Chen, H. Song, Boosting the electrical double-layer capacitance of graphene by self-doped defects through ball-milling, Adv. Funct. Mater. 29 (2019) 1901127, https://doi.org/10.1002/adfm.201901127.
[99] M. Zeiger, N. Jäckel, D. Weingarth, V. Presser, Vacuum or flowing argon: what is the best synthesis atmosphere for nanodiamond-derived carbon onions for supercapacitor electrodes? Carbon 94 (2015) 507–517, https://doi.org/10.1016/j.carbon.2015.07.028.
[100] D. Roy, M. Chhowalla, H. Wang, N. Sano, I. Alexandrou, T.W. Clyne, G.A. J. Amaratunga, Characterisation of carbon nano-onions using Raman spectroscopy, Chem. Phys. Lett. 373 (2003) 52–56, https://doi.org/10.1016/S0009-2614(03)00523-2.
[101] A. Krüger, F. Kataoka, M. Ozawa, T. Fujino, Y. Suzuki, A.E. Aleksenskii, A.Y. Vul', E. Ōsawa, Unusually tight aggregation in detonation nanodiamond: identification and disintegration, Carbon 43 (2005) 1722–1730, https://doi.org/10.1016/j.carbon.2005.02.020.
[102] M. Weng, Determination of the Hansen solubility parameters with a novel optimization method, J. Appl. Polym. Sci. 133 (2016), https://doi.org/10.1002/app.43328 n/a-n/a.
[103] G.C. Vebber, P. Pranke, C.N. Pereira, Calculating Hansen solubility parameters of polymers with genetic algorithms, J. Appl. Polym. Sci. 131 (2014), https://doi.org/10.1002/app.39696 app.39696.
[104] J. Howell, M. Roesing, D. Boucher, A functional approach to solubility parameter computations, J. Phys. Chem. B 121 (2017) 4191–4201, https://doi.org/10.1021/acs.jpcb.7b01537.
[105] S. Ata, T. Yamada, K. Hata, Relationship between primary structure and Hansen solubility parameter of carbon nanotubes, J. Nanosci. Nanotechnol. 17 (2017) 3310–3315, https://doi.org/10.1166/jnn.2017.13080.